An isogeometric FE-BE method and experimental investigation for the hydroelastic analysis of a horizontal circular cylindrical shell partially filled with fluid

M. Erden Yildizdag[a,*], I. Tugrul Ardic[a], Adnan Kefal[a], Ahmet Ergin[a]

[a]*Faculty of Naval Architecture and Ocean Engineering, Istanbul Technical University, Maslak, 34469, Istanbul, Turkey*

Abstract

In this study, the dynamic characteristics (i.e. natural frequencies and associated mode shapes) of a partially filled horizontal cylindrical shell are investigated experimentally and by an isogeometric finite element-boundary element method. The proposed numerical procedure is divided into two parts. In the first part, the dynamic characteristics of the cylindrical shell under in-vacuo conditions are obtained by the isogeometric finite element method (IGAFEM) based on a linear Kirchhoff-Love shell formulation. In the second part, the fluid-structure interaction effects are calculated in terms of generalized added mass coefficients by using the isogeometric boundary element method (IGABEM), assuming that the structure vibrates in its in-vacuo principle mode shapes. By adopting the linear hydroelasticity theory, it is assumed that the fluid flow is ideal, i.e., an incompressible flow and inviscid fluid. In order to show the versatility of the numerical method, the results are compared with those obtained by the conducted experiments. Relevant numerical challenges in the hydroelastic vibration analysis are highlighted and it is shown that the numerical predictions and experimental results are in good agreement.

Keywords: isogeometric analysis, hydroelasticity, finite element method,

---

[*]Corresponding author
Email address: `yildizdag@itu.edu.tr` (M. Erden Yildizdag)

Nomenclature

Ξ	Knot Vector
$\boldsymbol{\xi}$	2-D parameter space
N_i^p	B-spline basis functions
R_{ij}^{pq}	2-D Euclidean space
$\mathbf{s}_{ij}$	Position vector of control points
$\tilde{w}_{ij}$	Weights of control points
$\mathbf{S}$	Surface in 3-D Euclidean space
N_{cp}	Number of control points
n_{cp}	Number of control points of an element
Ω^e	Element domain in parameter space
$\mathbf{S}^e$	Element surface
x_1, x_2, x_3	Global rectangular Cartesian coordinates
$\theta^1, \theta^2, \theta^3$	Global rectangular Cartesian coordinates
$\mathbf{X}$	Position vector of a material point in shell body in undeformed configuration
$\mathbf{R}$	Position vector of a material point on mid-surface in undeformed configuration
$\mathbf{A}_3$	Director vector in undeformed configuration
$\mathbf{A}_\alpha$	Covariant base vectors of mid-surface in undeformed configuration
$\mathbf{x}$	Position vector of a material point in shell body in deformed configuration
$\mathbf{r}$	Position vector of a material point on mid-surface in deformed configuration
$\mathbf{a}_3$	Director vector in deformed configuration
$\boldsymbol{\theta}$	Rotation vector of the director vector representing its linearized rotation
$\mathbf{G}^i$	Contravariant base vectors of shell body
$\mathbf{G}_i$	Covariant base vectors of shell body
$\mathbf{u}$	Displacement vector of a material point in shell body
$\mathbf{v}$	Translational displacement vector of mid-surface
φ_α	Linearized rotation angles
$\boldsymbol{\varepsilon}$	Linearized Green-Lagrange strain tensor
$\mathbf{D}$	Reduced stiffness matrix of plane-stress condition
E	Young's modulus
ν	Poisson's ratio
h	Uniform thickness of shell body
$\mathbf{M}$	Global mass matrix
$\mathbf{K}$	Global stiffness matrix
$\mathbf{U}$	Vector of global displacements
ω	Natural frequency of the shell body
$\bar{\mathbf{U}}$	Amplitude of the modal displacements
$\bar{\mathbf{p}}$	Vector of principle coordinates
$\bar{\mathbf{D}}$	Modal matrix
$\mathbf{a}$	Normalized mass matrix
$\mathbf{b}$	Normalized stiffness matrix
$\mathbf{f}$	Velocity vector of a fluid particle
Φ	Velocity potential function
ϕ_k	Time-independent velocity potential due to structural deformations in k^{th} modal vibration
$\mathbf{x}_S$	Global Cartesian coordinates of source point
$\mathbf{x}_F$	Global Cartesian coordinates of field point
S_w	Wet surface area
S_i	Imaginary surface area
ρ_s	Density of the material of structure
ρ_f	Density of the fluid
A_{rk}	Generalized added mass due to the coupled vibration modes of r and k
F_{rk}	Generalized fluid-structure interaction forces due to the coupled vibration modes of r and k

boundary element method, experimental modal analysis

2010 MSC: 00-01, 99-00

---

1. Introduction

Dynamic response analysis of plates and shells has attracted the attention of researchers due to their wide range of applications in many engineering fields (for example, see [1–9]). Thin-walled structures interacting with fluid constitutes an important class of fluid-structure interaction problems. The presence of a fluid of comparable density significantly alters the dynamic characteristics of the structure compared to those in vacuo. This is due to the vibration of the structural surface in contact with the fluid medium imparting motion to the fluid, thus altering its pressure, and, hence inducing reactive forces on its surface.

The free vibration of cylindrical shells partially in contact with fluid has been of great interest to engineers and scientists for the last half century. One of the earlier pioneering work in this field was performed by Warburton [10] using an analytical approach, where the cylindrical shell is either filled with fluid or submerged into an infinite fluid domain. Lindholm et al. [11] conducted an experimental study to predict the natural frequencies of partially fluid-filled vertical cylindrical shells. In a number of further studies, researchers investigated the effect of fluid on the dynamic response characteristics of thin and thick cylindrical shells (for example, see Zhang et. al. [12], Wang et al. [13], and Ji et al. [14]) by using analytical approaches. There are also studies using the wave propagation approach and Fourier series expansion method (for example, see Zhang [15], Jeong and Lee [16], Jeong [17]). Recently, the free vibration characteristics of fluid-filled composite cylindrical shells were investigated analytically, for instance, by Thinh and Nguyen [18] and Izyan et al. [19].

Additionally, semi-analytical approaches have also been used in combination with various shell theories and fluid-structure interaction models. In these studies, the wet natural frequencies and the corresponding mode shapes were often obtained by using the Rayleigh-Ritz (Ergin [20], Amabili [21], Askari and Jeong [22]) and Galerkin (Chiba et al. [23], Amabili [24, 25]) methods. Furthermore, Gonçalves and Ramos [26] utilized the reduced linear form of Sander's shell theory, where the fluid motion is governed by the Laplace's equation in cylindrical coordinates. In this study, the effect of linearized free surface condition was also included into the mathematical model and the resulting linearized system of differential equations was solved by Galerkin error minimization procedure. Liao et al. [27] investigated the vibration and sound radiation characteristics of reinforced cylindrical shells in an acoustic medium by using a method based on modal analysis procedure. In the study, based on the work of Laulagnet and Guyader [28], the effect of fluid was represented by a series expansion of acoustic pressure. Recently, Chiba and Magata [29] used the Rayleigh-Ritz method to obtain the dynamic characteristics of a beam-rigid tank-fluid coupled system.

Utilization of numerical methods in fluid-structure interaction problems has become more and more important with everyday increasing computer power, as analytical approaches are only applicable for some basic geometries and considerably simplified cases. The finite element method (FEM) has found wide application in vibration problem of shell structures in contact with fluid (for example, see Bochkarev et al. [30, 31]). Hybrid finite element methods, in which approximation functions are directly derived from classical shell theories, have been implemented in several studies. For instance, Lakis et al. [32] investigated the dynamic response characteristics of partially liquid-filled horizontal cylindrical shells by using a hybrid finite element formulation based on Sander's shell theory. The obtained results were compared with those computed by Selmane and Lakis [33], which is based on the same approach but without including the free surface effects. In a further study, Sabri and Lakis [34] investigated the dynamic responses of horizontal cylindrical shells partially in contact with fluid under internal pressure and axial compression.

On the other hand, the boundary element method (BEM) has found wide application in fluid-structure interaction problems due to its inherent advantages, especially in modeling of fluid domain. In hydroelastic vibration problems, BEM is generally used to model fluid-structure interaction effects in conjunction with the structural model solved via FEM (for example, see Ergin et al. [35], Ventsel et al. [36], Yildizdag et al. [37]). In this context, Ergin and Temarel [38] analyzed the free vibration characteristics of a horizontal circular cylindrical shell, which is partially liquid-filled and/or submerged, by a combined FE-BE method. Zheng et al. [39] performed the free vibration analysis of spherical and cylindrical shells by a FE-BE method.

The isogeometric analysis (IGA) is a computational approach forming a direct connection between numerical analysis and computer aided design (CAD) by using the same basis functions. In this concept, overall computational domain directly matches to the geometry generated in CAD. The IGA-based numerical procedures were first applied to the structural problems and have been steadily developed due to its advantages over classical FEM-based numerical tools. Following the pioneering work of Hughes and his co-workers [40], the concept of isogeometric analysis proceeded with significant promise in various fields such as elastostatics (Cazzani et al. [41–44], Kefal et al. [45], Yildizdag et al. [46], Hasim et al. [47]), contact problems (Temizer [48], Nishi et al. [49]), bioengineering (Bartezzaghi et. al. [50]), turbulent flow (Bastl et al. [51]), vibration analysis (Chen et al. [52], Xue et al. [53]) and acoustics (Jin et al. [54]). Recently, Khakalo and Niiranen [55]have been successully applied IGA for higher-order gradient elasticity problems (Alibert et al. [56], dell'Isola [57], Giorgio et al. [58], dell'Isola et al. [59, 60]). As for the developments in hydrodynamics, Maestre et al. [61] used three-dimensional isogeometric boundary element method (IGABEM) to model nonlinear free surface gravity waves. Kostas et al. [62] utilized IGABEM to optimize the shapes of 2D hydrofoils. To assess the degree of confidence of IGABEM in the calculation of wave resistance of ships, Wang et al. [63] conducted a comparative study with a commercial CFD solver.

The main objective of this study is to present an isogeometric FE-BE method for analyzing the free vibration characteristics of a partially filled horizontal circular cylindrical shell. Furthermore, an experimental study is also conducted to measure the natural frequencies and associated mode shapes. The main novelty of this study is the proposed numerical model using the isogeometric concept in both FE and BE formulations. According to a deep literature review, there is no other study found employing the IGA concept into both formulations for the hydroelastic analysis of shell structures partially in contact with fluid. In this context, the numerical framework to analyze the fluid-structure interaction system is divided into two parts. The dry analysis involves obtaining the natural frequencies and corresponding mode shapes of the cylindrical shell under in-vacuo conditions. Then, in the wet analysis, the fluid flow is considered as ideal, i.e. incompressible flow and inviscid fluid. In the formulation, it is assumed that each in-vacuo principal mode contributes to the total radiation potential, and the instantaneous pressure acting on the wetted part of the structure is determined from the linearized form of the Bernoulli equation. Furthermore, free surface waves are neglected by assuming that the structure vibrates in high frequency region, so that the hydrodynamic forces are associated only with the inertial effect of fluid in terms of the generalized added mass coefficients. Therefore, the mathematical model for the cylindrical shell is combined with the generalized added mass matrix, and the wet resonant frequencies and corresponding mode shapes are obtained by solving this coupled eigenvalue problem. The natural frequencies and corresponding mode shapes are compared with those obtained from the experiments performed in this study. In addition, the calculated in-vacuo and wet dynamic characteristics are validated with those obtained by a commercial FEM software, ANSYS®. In order to assess the influence of fluid filling ratio on the natural frequencies and mode shapes, a number of further studies is performed experimentally and numerically. The results clearly reveal that the isogeometric FE-BE procedure can determine the dynamic response behavior of fluid-coupled shell structures in the presence of free surface, with excellent precision.

The organization of the rest of the paper is as follows: In Section 2, the isogeometric FE-BE procedure is presented in detail. In Section 3, the experimental setup and conducted measurements are briefly explained. The numerical results obtained by the proposed numerical framework is presented and compared with those obtained by experiments and ANSYS for the horizontal cylindrical circular shell under study in Section 4. Finally, in Section 5, the conclusions are drawn.

2. Mathematical Formulation of Isogeometric FE-BE Model

2.1. Non-Uniform Rational B-Splines (NURBS)

Isogeometric Analysis (IGA) [40] unifies the design and analysis environments through utilization of non-uniform rational B-splines (NURBS) basis functions to describe the structural geometry and physical unknown fields, e.g., displacements for solid mechanics problems. The main advantage of using NURBS basis function is that it can be easily enabled to model exact physical geometry and provides basic mesh refinement via smooth interpolations. A large collection of literature [64, 65] has already established the mathematical preliminaries of the NURBS and B-Splines, thus only a brief introduction is provided herein to constitute a clear notation in the rest of the study.

A B-spline curve can be defined using a set of control points and a one-dimensional knot vector. For a given curved geometry, the control points do not necessarily need to conform the actual physical geometry, they rather behave like a scaffold or control mesh that controls the shape of the geometry. Therefore, the coordinates of a point cloud defined in the three-dimensional rectangular Cartesian coordinate system represent the control points. On the other hand, a non-decreasing coordinates of the one-dimensional parameter space, ξ, defines the knot vector as $\Xi = \{\xi_1, \xi_2, \ldots, \xi_{n-p-1}\}$ where ξ_i is the ith knot, n is the number of basis functions, and p is the polynomial order (degree). For a given Ξ vector, the B-spline basis functions, $N_i^p(\xi)$, can be defined through the Cox-de Boor recursive formula for $p = 0$

$$N_i^0(\xi) = \begin{cases} 1 & \text{if } \xi_1 \leq \xi < \xi_{i+1}, \\ 0 & \text{otherwise}, \end{cases} \tag{1}$$

and for $p > 0$

$$N_i^p(\xi) = \frac{\xi - \xi_i}{\xi_{i+p} - \xi_i} N_i^{p-1}(\xi) + \frac{\xi_{i+p+1} - \xi}{\xi_{i+p+1} - \xi_{i+1}} N_{i+1}^{p-1}(\xi). \tag{2}$$

Each repetition of any knot in the interior of a knot vector locally decreases the degree of continuity by one. Thus, B-splines provide C^{p-m} continuity across the knots, where m represents the multiplicity of the knots in Ξ vector. Additionally, the B-spline basis functions constitute a partition of unity and are pointwise non-negative. Essentially, the NURBS can be considered as the B-splines in homogeneous coordinates. From a geometric point of view, the NURBS are obtained by projective transformation of B-splines from $\mathbb{R}^{d+1}$ to $\mathbb{R}^{d}$ through utilizing geometric weights defined at each control point. Therefore, the NURBS basis function has a generalized mathematical form of the B-splines, such that setting the weights of each control point to unity, a NURBS becomes identical to a B-spline. A surface, $\mathbf{S}(\xi, \eta)$, in three-dimensional Euclidean space $\mathbb{R}^3$ can be constructed from a linear combination of two-dimensional NURBS basis functions, $R_{ij}^{pq}(\xi, \eta)$, control points, $\mathbf{s_{ij}} \in \mathbb{R}^{\mathbf{3}}$, and associated weights, w_{ij}, as

$$\mathbf{S}(\xi, \eta) = \sum_{i=1}^{n} \sum_{j=1}^{m} R_{ij}^{pq}(\xi, \eta)\mathbf{s}_{ij} \tag{3}$$

where the NURBS basis functions are defined as

$$R_{ij}^{pq}(\xi, \eta) = \frac{N_i^p(\xi) M_i^q(\eta) w_{ij}}{\sum_{k=1}^{n} \sum_{l=1}^{m} N_k^p(\xi) M_i^q(\eta) w_{kl}}. \tag{4}$$

Alternatively, mapping of the surface given in Eq. 4 can be written more concisely as

$$\mathbf{S}(\boldsymbol{\xi}) = \sum_{A=1}^{N_{cp}} R_A(\boldsymbol{\xi})\mathbf{s}_A \tag{5}$$

where $\boldsymbol{\xi}$ represents the two-dimensional parameter space, (ξ, η), $A = n(j-1)+i$ interrelates the local ij subscript with a global one, and number of global control points is calculated as $N_{cp} = n \times m$. In addition, the pq superscript denoting the order of the individual B-splines is removed for brevity of the notation. The locations of the knot define the boundaries of isogeometric elements in the parametric space. Hence, the non-zero parametric region bounded by the line of unique (non-repeating) knots constitutes an element domain as $\Omega^e = [\xi_i, \xi_{i+1}] \times [\eta_j, \eta_{j+1}]$ with $\xi_i \neq \xi_{i+1}$ and $\eta_j \neq \eta_{j+1}$ for any i and j knot. Then, the physical surface corresponding to the element domain can be written as

$$\mathbf{S}^e(\boldsymbol{\xi}) = \sum_{a=1}^{n_{cp}} R_a^e(\boldsymbol{\xi})\mathbf{s}_a \quad (e = 1, 2, ..., n_{el}) \tag{6}$$

where $n_{el} = (n - p)(m - p)$ is total number element available on S surface, $\mathbf{s}_a$ represents the control points belong to an element with $a = 1, 2, ..., n_{cp}$ index being the local identities of the control points, and $n_{cp} = (p + 1)(q + 1)$ is the total number of control points of the element. In the rest of the study, in addition to the geometry discretization, we will utilize NURBS basis functions to approximate the main unknown fields (e.g. displacement of the structure and velocity potential of fluid) of the hydroelastic vibration problem.

2.2. Isogeometric Finite Element Formulation

2.2.1. Shell Kinematics and Differential Geometry

To establish a compact notation in the remainder of the mathematical model, unless otherwise specified, indices α and β range from one to two. Consider an arbitrary curved shell body with a uniform thickness h that is at least two order of magnitude smaller than the characteristic dimension of the body such as span or diameter. General convected curvilinear coordinate system $(\theta^1, \theta^2, \theta^3)$ is used to identify a material point of the curved shell body. The in-plane (surface) coordinates are represented by $\theta^\alpha \in S$, where S denotes the area of the mid-surface. The coordinate $\theta^3 \in [-h/2, +h/2]$ identifies the thickness direction of the shell and material points located at the mid-surface of the shell are described as $\theta^3 = 0$. In addition to curvilinear coordinate system, a fixed rectangular cartesian coordinate system (x_1, x_2, x_3) is utilized to describe orthogonal position of the points. The (x_1, x_2, x_3) system has orthonormal basis $(\mathbf{e}_1, \mathbf{e}_2, \mathbf{e}_3)$ pointing the direction of the coordinate axes as shown in Fig. 1. The position vector $\mathbf{X}$ is attributed to the position of the arbitrary material points in undeformed configuration of the shell body. This vector can be written as a linear function of θ^3 coordinate

$$\mathbf{X}(\theta^1, \theta^2, \theta^3) = \mathbf{R}(\theta^1, \theta^2) + \theta^3\mathbf{A}_3(\theta^1, \theta^2) \tag{7}$$

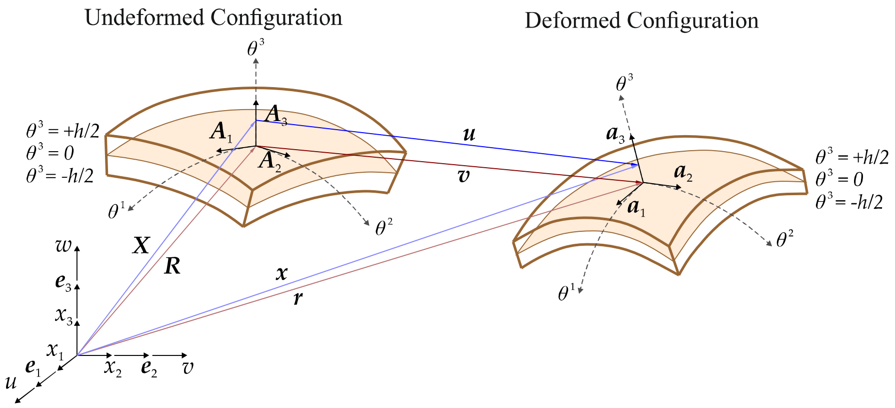

Figure 1: Kinematics of shell body in undeformed and deformed configurations

where $\mathbf{R}$ represents the position vector to a material point on the mid-surface in reference configuration and $\mathbf{A}_3$ denotes the unit-magnitude vector field (the director vector) that is perpendicular to the tangent plane of any point belongs to mid-surface in reference configuration (Fig. 1). Taking partial derivative of $\mathbf{R}$ with respect to θ^α provides the covariant base vectors $\mathbf{A}_\alpha$ of the mid-surface in reference configuration as $\mathbf{A}_\alpha = \mathbf{R}_{,\alpha}$. Normalized cross product of the $\mathbf{A}_\alpha$ covariant base vectors can be utilized to define the director vector as follows

$$\mathbf{A}_3 = \frac{\mathbf{A}_1 \times \mathbf{A}_2}{\|\mathbf{A}_1 \times \mathbf{A}_2\|}. \tag{8}$$

The position vector $\mathbf{x}$ of any material point in deformed configuration of the shell body can be described analogous to Eq. 7 as

$$\mathbf{x}(\theta^1, \theta^2, \theta^3) = \mathbf{r}(\theta^1, \theta^2) + \theta^3 \mathbf{a}_3(\theta^1, \theta^2) \tag{9}$$

where $\mathbf{r}$ is the position vector to a material point on the mid-surface and $\mathbf{a}_3$ is the director vector in deformed configuration (Fig. 1). According to the thin shell model of Etcher et al. [66] developed based on Kirchhoff-Love shell kinematics, the director vector $\mathbf{a}_3$ can be defined by linearized rotation of the director vector $\mathbf{A}_3$ as

$$\mathbf{a}_3 = \mathbf{A}_3 + \boldsymbol{\theta} \times \mathbf{A}_3 \tag{10}$$

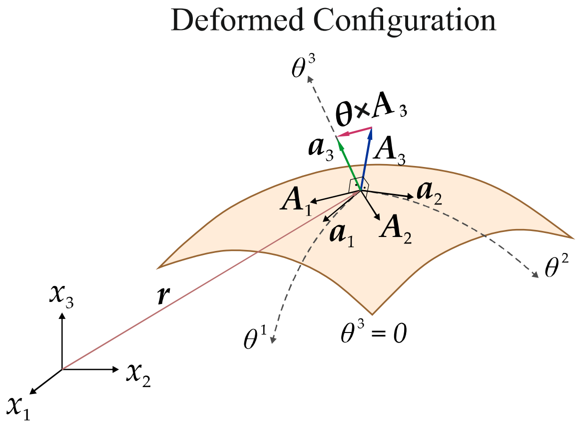

Figure 2: The effect of rotation vector during deformation of shell body.

where $\boldsymbol{\theta}$ is the rotation vector and $\boldsymbol{\theta} \times \mathbf{A}_3$ represents the rotational difference between the directors of the reference and current configurations as depicted in Fig. 2. Subtracting the position vector of undeformed configuration from the position vector of deformed configuration, displacement vector $\mathbf{u}$ of any arbitrary point in the shell body can be defined as

$$\mathbf{u} = \mathbf{x} - \mathbf{X} = \mathbf{v} + \theta^3(\boldsymbol{\theta} \times \mathbf{A}_3) \tag{11}$$

where $\mathbf{v}$ is mid-surface displacement vector representing the translational displacements of the mid-surface of the shell body. The orthogonal components of this vector can be explicitly defined as $\mathbf{v} = [u, v, w]^T$ where the functions $u \equiv u(\theta^1, \theta^2), v \equiv v(\theta^1, \theta^2)$, and $w \equiv w(\theta^1, \theta^2)$ represent translations along the x_1, x_2, and x_3 coordinates, respectively (Fig. 1). In addition, the rotation vector $\boldsymbol{\theta}$ can be described in terms of in-plane covariant base vectors $\mathbf{A}_\alpha$ and related rotation angles ϕ_α as [66]

$$\boldsymbol{\theta} = \varphi_1 \mathbf{A}_1 + \varphi_2 \mathbf{A}_2 \tag{12}$$

with

$$\varphi_1 = \frac{\mathbf{v}_{,2} \cdot \mathbf{A}_3}{\|\mathbf{A}_1 \times \mathbf{A}_2\|} \quad \text{and} \quad \varphi_2 = \frac{-\mathbf{v}_{,1} \cdot \mathbf{A}_3}{\|\mathbf{A}_1 \times \mathbf{A}_2\|}, \tag{13}$$

where the rotation vector $\boldsymbol{\theta}$ is a function of $\mathbf{v}_{,\alpha}$. Therefore, the orthogonal components of the $\mathbf{v}$ vector are the only unknowns (namely, the kinematic variables) during the analysis in order to predict the $\mathbf{u}$ displacements of any material point in the shell body.

The linearized Green-Lagrange strain tensor can be defined with respect to the convected curvilinear coordinates as

$$\boldsymbol{\varepsilon} = \varepsilon_{ij}\,\mathbf{G}^i \otimes \mathbf{G}^j \tag{14}$$

where $\mathbf{G}^i$ denotes the contravariant base vectors and the coefficients ε_{ij} of strain tensor are defined in terms of covariant base vectors, $\mathbf{G}_i$, of the shell body as

$$\varepsilon_{ij} = \frac{1}{2}\left(\mathbf{u}_{,i} \cdot \mathbf{G}_j + \mathbf{u}_{,j} \cdot \mathbf{G}_i\right) \tag{15}$$

with

$$\mathbf{G}_\alpha = \mathbf{X}_{,\alpha} = \mathbf{A}_\alpha + \theta^3 \mathbf{A}_{3,\alpha} \quad \text{and} \quad \mathbf{G}_3 = \mathbf{X}_{,3} = \mathbf{A}_3 \tag{16}$$

Once the covariant base vectors are evaluated for a position $\mathbf{X}$ in the shell domain, the contravariant base vectors $\mathbf{G}^i$ can be calculated for the same location as $\mathbf{G}^i = G^{ij}\mathbf{G}_j$ where the contravariant components G^{ij} of the metric tensor are obtained by taking the inverse of the covariant tensor components, $G_{ij} = \mathbf{G}_i \cdot \mathbf{G}_j$. For clarity of the Eq. 16, the derivatives of the director vector with respect to in-plane curvilinear components can be explicitly written as

$$\mathbf{A}_{3,\alpha} = \frac{1}{\|\mathbf{A}_1 \times \mathbf{A}_2\|}\Big(\mathbf{A}_{1,\alpha} \times \mathbf{A}_2 + \mathbf{A}_1 \times \mathbf{A}_{2,\alpha} - \mathbf{A}_3\Big[\mathbf{A}_{1,\alpha} \cdot (\mathbf{A}_2 \times \mathbf{A}_3) + \mathbf{A}_{2,\alpha} \cdot (\mathbf{A}_3 \times \mathbf{A}_1)\Big]\Big). \tag{17}$$

Taking derivatives of the $\mathbf{u}$ displacement and subsequently substituting these derivatives into Eq. 15, the ε_{ij} strains can be explicitly defined as

$$\varepsilon_{11} = \mathbf{v}_{,1} \cdot \mathbf{A}_1 + \theta^3\Big(\mathbf{v}_{,1} \cdot \mathbf{A}_{3,1} + (\mathbf{A}_3 \times \mathbf{A}_1) \cdot \boldsymbol{\theta}_{,1}\Big), \tag{18}$$

$$\varepsilon_{22} = \mathbf{v}_{,2} \cdot \mathbf{A}_2 + \theta^3\Big(\mathbf{v}_{,2} \cdot \mathbf{A}_{3,2} + (\mathbf{A}_3 \times \mathbf{A}_2) \cdot \boldsymbol{\theta}_{,2}\Big), \tag{19}$$

$$2\varepsilon_{12} = \gamma_{12} = \mathbf{v}_{,1} \cdot \mathbf{A}_2 + \mathbf{v}_{,2} \cdot \mathbf{A}_1 + \theta^3\Big(\mathbf{v}_{,1} \cdot \mathbf{A}_{3,2} + \mathbf{v}_{,2} \cdot \mathbf{A}_{3,1} + (\mathbf{A}_3 \times \mathbf{A}_2) \cdot \boldsymbol{\theta}_{,1} + (\mathbf{A}_3 \times \mathbf{A}_1) \cdot \boldsymbol{\theta}_{,2}\Big), \tag{20}$$

$$2\varepsilon_{\alpha 3} = \gamma_{\alpha 3} = \mathbf{u}_{,\alpha} \cdot \mathbf{G}_3 + \mathbf{u}_{,3} \cdot \mathbf{G}_\alpha = 0. \tag{21}$$

Note that, during the derivation of the Eqs. 18-21, all strain contributions of $(\boldsymbol{\theta} \times \mathbf{A}_{3,\alpha}) \cdot \mathbf{A}_\beta$ vanish identically because the vectorial quantities obtained from the cross products of $\boldsymbol{\theta}$ and $\mathbf{A}_{3,\alpha}$ are normal to the mid-surface of the shell body. In addition, as given in Eq. 21, the Kirchhoff-Love shell model exhibits zero transverse-shear strains, $\gamma_{\alpha 3} = 0$, indicating that the deformations of the shell body will be physically dictated by only membrane and bending actions.

For clarity of the strain definition for computational implementation, the explicit form of the derivatives of rotation vector with respect to coordinates are written as

$$\boldsymbol{\theta}_{,\alpha} = \varphi_{1,\alpha}\mathbf{A}_1 + \varphi_1\mathbf{A}_{1,\alpha} + \varphi_{2,\alpha}\mathbf{A}_2 + \varphi_2\mathbf{A}_{2,\alpha}. \tag{22}$$

Applying plane-stress condition (i.e., zero normal stress, $\sigma_{33} = 0$, along the thickness coordinate, θ^3) to Hooke's stress-strain relations of a linear elastic and isotropic material, the constitutive model according to the Cartesian coordinates of the shell body can be defined using the Voigt notation as $\hat{\boldsymbol{\sigma}} = \mathbf{D}\hat{\boldsymbol{\varepsilon}}$ where the in-plane strains and stresses are written as

$$\hat{\boldsymbol{\varepsilon}} = \begin{bmatrix} \varepsilon_{11} & \varepsilon_{22} & \gamma_{12} \end{bmatrix}^T \quad \text{and} \quad \hat{\boldsymbol{\sigma}} \begin{bmatrix} \sigma_{11} & \sigma_{22} & \tau_{12} \end{bmatrix}^T, \tag{23}$$

and reduced stiffness matrix can be written as

$$\mathbf{D} = \frac{E}{1-\nu^2} \begin{bmatrix} (G^{11})^2 & \nu G^{11}G^{22} + (1-\nu)(G^{12})^2 & G^{11}G^{12} \\ & (G^{22})^2 & G^{22}G^{12} \\ \text{sym} & & \frac{1}{2}\left((1-\nu)G^{11}G^{22} + (1+\nu)(G^{12})^2\right) \end{bmatrix} \tag{24}$$

with the material coefficients being transformed from local (curvilinear) to global (Cartesian) coordinates. The contravariant metric coefficients of the shell mid-surface are utilized for this transformation since the present shell model accounts for thin shell bodies. Accordingly, these coefficients can be calculated as

$$\begin{bmatrix} G^{11} & G^{12} \\ G^{12} & G^{22} \end{bmatrix} = \begin{bmatrix} \mathbf{A_1} \cdot \mathbf{A_1} & \mathbf{A_1} \cdot \mathbf{A_2} \\ \mathbf{A_1} \cdot \mathbf{A_2} & \mathbf{A_2} \cdot \mathbf{A_2} \end{bmatrix}^{-1}. \tag{25}$$

2.2.2. Rotation-Free Isogeometric Kirchhoff-Love Shell Element

Both position vector of shell mid-surface, $\mathbf{R}$, and kinematic variables of the shell, $\mathbf{v}$, are the only functions of the surface coordinates, θ^α (refer to Eq. 7). Hence, the NURBS basis functions can be readily utilized to approximate both these geometrical and analysis terms while establishing an analogy between the curvilinear and parametric coordinates, i.e., $\boldsymbol{\xi} \equiv (\xi, \eta) \equiv (\theta^1, \theta^2)$, as

$$\mathbf{R}(\boldsymbol{\xi}) = \sum_{i=1}^{n_{cp}} R_i^e(\boldsymbol{\xi})\mathbf{P}_i = \begin{bmatrix} R_1^e(\boldsymbol{\xi})\mathbf{I} & \dots & R_{n_{cp}}^e(\boldsymbol{\xi})\mathbf{I} \end{bmatrix} \begin{Bmatrix} \mathbf{P}_1 \\ \vdots \\ \mathbf{P}_{n_{cp}} \end{Bmatrix} = \mathbf{N}^e\mathbf{P}^e \tag{26}$$

and

$$\mathbf{v}(\boldsymbol{\xi}) = \sum_{i=1}^{n_{cp}} R_i^e(\boldsymbol{\xi})\mathbf{v}_i = \begin{bmatrix} R_1^e(\boldsymbol{\xi})\mathbf{I} & \dots & R_{n_{cp}}^e(\boldsymbol{\xi})\mathbf{I} \end{bmatrix} \begin{Bmatrix} \mathbf{v}_1 \\ \vdots \\ \mathbf{v}_{n_{cp}} \end{Bmatrix} = \mathbf{N}^e\mathbf{v}^e \tag{27}$$

where the $\mathbf{N}^e \equiv \mathbf{N}(\boldsymbol{\xi})$ matrix, and the $\mathbf{P}^e$ and $\mathbf{v}^e$ vectors represent the $3 \times (3 \times n_{cp})$ matrix of NURBS basis functions, and the $(3 \times n_{cp}) \times 1$ position and displacement degrees-of-freedom (DOF) vectors of control points belonging to an individual isogeometric shell element, respectively. As depicted in Fig. 3, the $\mathbf{P}_i$ and $\mathbf{v}_i$ vectors given in Eqs. 26 and 27 denote the position and displacement DOF of ith control point, respectively. Thanks to the high-order continuity provided by NURBS basis functions, there is no need to allocate an extra DOF for the rotations of the shell, which can be directly incorporated into the kinematics as the first-order derivatives of the $\mathbf{v}(\boldsymbol{\xi})$ vector. Note that the direction of displacement DOF are aligned with the components of the Cartesian coordinate system and the positions of control points are defined with respect to the same system.

Substituting Eqs. 26 and 27 into strain definition, the in-plane strains given in Eq. 23 can be written in the compact discrete form for an individual isogeometric element as

$$\hat{\boldsymbol{\varepsilon}} = \mathbf{m}(\mathbf{v}^e) + \theta^3\mathbf{b}(\mathbf{v}^e) = \left(\mathbf{B}_m^e + \theta^3\mathbf{B}_b^e\right)\mathbf{v}^e \tag{28}$$

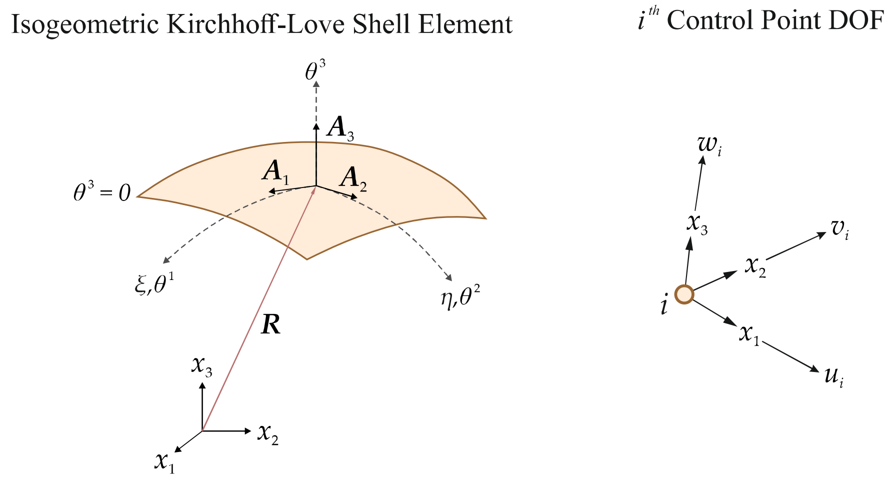

Figure 3: Isogeometric shell element and its displacement DOF for ith control point.

where $\mathbf{m}(\mathbf{v}^e)$ is the membrane strains associated with stretching of the mid-surface, $\mathbf{b}(\mathbf{v}^e)$ is the bending curvatures of the mid-surface, and the matrices $\mathbf{B}^e_m$ and $\mathbf{B}^e_b$ are the corresponding strain-displacement relation matrices.

2.2.3. In-vacuo analysis

To account for the free vibrations of the in-vacuo shell body, we employ principle of virtual work utilizing the classical weak form of the equations of motion. Accordingly, sum of the virtual works done by the inertial and internal forces become equal to zero as:

$$\delta W^I + \delta W^{II} = 0 \tag{29}$$

where the virtual work corresponding to inertia forces can be written in a compact matrix-vector form as

$$\begin{aligned} \delta W^I = \int\limits_V \rho_s \, \delta \mathbf{u}^T \ddot{\mathbf{u}} \, dV &\simeq \int\limits_V \rho_s \, \delta \mathbf{v}^T \ddot{\mathbf{v}} \, dV \\ &= \delta(\mathbf{v}^e)^T \left(\rho_s \, t \int\limits_{S^e} (\mathbf{N}^e)^T \mathbf{N}^e \right) \ddot{\mathbf{v}}^e \\ &= \delta(\mathbf{v}^e)^T \mathbf{m}^e \ddot{\mathbf{v}}^e \end{aligned} \tag{30}$$

and similarly the virtual work done by internal forces can be defined as

$$\begin{aligned}\delta W^{II} &= \int\limits_V \delta\hat{\boldsymbol{\varepsilon}}^T \hat{\boldsymbol{\sigma}}\, dV \\ &= \delta(\mathbf{v}^e)^T \left(h \int\limits_{S^e} (\mathbf{B}_m^e)^T \mathbf{D}\mathbf{B}_m^e \, dS^e + \frac{h^3}{12} \int\limits_{S^e} (\mathbf{B}_b^e)^T \mathbf{D}\mathbf{B}_b^e \, dS^e \right) \mathbf{v}^e \\ &= \delta(\mathbf{v}^e)^T \mathbf{k}^e \mathbf{v}^e \end{aligned} \tag{31}$$

where V denotes the volume of the shell body and S^e represents the mid-surface area of an isogeometric shell element. In Eqs. 30 and 31, the $\mathbf{m}^e$ and $\mathbf{k}^e$ matrices stand for mass and stiffness matrices of a thin isogeometric shell element, respectively. The area integrations given in Eqs. 30 and 31 can be performed numerically by using, for instance, Gauss quadrature method. For this purpose, two subsequent domain transformation is required: (1) from physical domain to parameter domain, $S^e \to \Omega^e$, and (2) from parameter domain to parent domain, $\Omega^e \to \tilde{\Omega}^e$, where parent domain is defined as $\tilde{\Omega}^e = [-1, +1] \otimes [-1, +1]$. Hence, two different Jacobian matrices associated with these transformations should be established for each isogeometric element. For conciseness of the mathematical derivations, the details of defining Jacobian matrices are not given herein. Further details can be readily implemented in accordance with classical IGA procedures [67].

Substituting Eqs. 30 and 31 into Eq. 29, a set of algebraic equations is obtained to solve the free vibration problem of an isogeometric element as:

$$\delta W^I + \delta W^{II} = \delta(\mathbf{v}^e)^T \left(\mathbf{m}^e \ddot{\mathbf{v}}^e + \mathbf{k}^e \mathbf{v}^e \right) = 0 \quad \Rightarrow \quad \mathbf{m}^e \ddot{\mathbf{v}}^e + \mathbf{k}^e \mathbf{v}^e = 0. \tag{32}$$

For a given isogeometric discretization (i.e., composed of n_{el} number of element contributions) can be assembled into a global set of final equations as:

$$\mathbf{M}\ddot{\mathbf{U}} + \mathbf{K}\mathbf{U} = \mathbf{0}. \tag{33}$$

where the $\mathbf{M}$ and $\mathbf{K}$ matrices are the global mass and stiffness matrices of the discretization, and $\mathbf{U}$ vector is the global displacement DOF of the whole structure. Here, we are interested in finding natural frequencies and modal displacements of the discretization. For harmonic vibration of a free and undamped structure, the time-dependent displacements can be expressed as

$$\mathbf{U}(t) = \bar{\mathbf{U}} e^{i\omega t} \tag{34}$$

where the $i = \sqrt{-1}$ term represents the complex number, ω is natural frequency of the shell body, and $\bar{\mathbf{U}}$ is the amplitude of the modal displacements which is only a function of spatial variable $\mathbf{X}$. Substituting the trial solution given by Eq. 34 into Eq. 33 and eliminating the common exponential term yields to

$$\left(\mathbf{K} - \lambda \mathbf{M}\right) \bar{\mathbf{U}} = \mathbf{0} \quad (\lambda = \omega^2) \tag{35}$$

which can be solved through eigenvalue decomposition, thus resulting in N_m number of roots $\lambda := \{\lambda_1, \lambda_2, \dots, \lambda_{N_m}\}$, i.e., the so-called "eigenvalues", for each of which an "eigenvector" is also obtained, $\bar{\mathbf{U}} = \{\bar{\mathbf{U}}_1, \bar{\mathbf{U}}_2, \dots, \bar{\mathbf{U}}_{N_m}\}$. Herein, the term N_m represents the total number of modes of interest, which can be elevated up to total degrees-of-freedom of the system, $3 \times N_{cp}$. Note that the physical counterpart of eigenvalues are the square of each natural frequency of the modal vibration while the each corresponding eigenvector represents the vibration mode. In fact, the cluster of eigenvectors is dynamically uncoupled and linear superposition of these vectors can be utilized to describe the modal displacements as

$$\bar{\mathbf{U}} = \bar{\mathbf{U}}_1 \bar{p}_1 + \bar{\mathbf{U}}_1 \bar{p}_2 + \cdots + \bar{\mathbf{U}}_{N_m} \bar{p}_{N_m} = \bar{\mathbf{D}} \bar{\mathbf{p}} \tag{36}$$

where the term $\bar{p}_k (k = 1, 2, \dots, N_m)$ represents the kth principle (natural) coordinates of modal vibration, the term $\bar{\mathbf{p}}$ is the vector of principle coordinates, and $\bar{\mathbf{D}}$ is the modal matrix with size of $(3 \times N_{cp}) \times N_m$, whose columns consist of eigenvectors, $\bar{\mathbf{U}}_k$. For clarity, the eigenvector of kth modal vibration can be explicitly expressed as

$$\bar{\mathbf{U}}_k = \begin{bmatrix} \bar{\mathbf{v}}_{k_1} & \bar{\mathbf{v}}_{k_2} & \cdots & \bar{\mathbf{v}}_{k_{N_{cp}}} \end{bmatrix}^T \tag{37}$$

with

$$\bar{\mathbf{v}}_{k_i} = \begin{bmatrix} \bar{u}_i & \bar{v}_i & \bar{w}_i \end{bmatrix}^T \quad (i = 1, 2, \dots, N_{cp}; k = 1, 2, \dots, N_m) \tag{38}$$

where the $\bar{\mathbf{v}}_{k_i}$ is vector of modal displacements of kth vibration mode at the control point i. Substituting Eq. 36 into Eq. 35 and pre-multiplying the resulting equation from left-hand-side by $\bar{\mathbf{D}}^T$ matrix, a generalized form of the equation of motion for vibration analysis can be obtained as

$$\left(\mathbf{b} - \omega^2 \mathbf{a}\right) \bar{\mathbf{p}} = 0 \tag{39}$$

where $\mathbf{a}$ and $\mathbf{b}$ denote generalized mass and stiffness matrices, respectively, which are defined as

$$\mathbf{a} = \bar{\mathbf{D}}^T \mathbf{M} \bar{\mathbf{D}} \quad \text{and} \quad \mathbf{b} = \bar{\mathbf{D}}^T \mathbf{K} \bar{\mathbf{D}} \tag{40}$$

If the mass normalization is enforced on the modal displacements for kth vibration mode, $\bar{\mathbf{U}}_k^T \mathbf{M} \bar{\mathbf{U}}_k = 1$, then $\mathbf{a} = \mathbf{I}$ matrix become an identity matrix, and accordingly $\mathbf{b} = \mathbf{\Lambda}$ matrix will be formed as the diagonal matrix of squared frequencies of the system as

$$\mathbf{\Lambda} = \begin{bmatrix} \omega_1^2 & & \\ & \ddots & \\ & & \omega_{N_m}^2 \end{bmatrix} \tag{41}$$

which automatically satisfies Eq. 39 and enables to obtain mass normalized modal displacement.

2.3. Isogeometric Boundary Element Formulation

Assuming an ideal fluid flow, velocity vector $\mathbf{f} = \mathbf{f}(\mathbf{X}, t)$ of a fluid particle due to structural vibration can be expressed in terms of the gradient of the velocity potential function, $\Phi(\mathbf{X}, t)$, as

$$\mathbf{f} = \nabla \Phi(\mathbf{X}, t) \tag{42}$$

where $\mathbf{X}$ is the vector attributed to the position of the fluid particle with respect to the origin of Cartesian coordinate system (x_1, x_2, x_3) throughout the fluid domain. When a structure is under vibration with a frequency of ω in the fluid domain, the velocity potential functional due to structural displacements in kth modal vibration can be written as

$$\Phi_k(\mathbf{X}, t) = \mathrm{Re}\{i\omega\phi_k(\mathbf{X})\bar{p}_k e^{i\omega t}\} \quad (k = 1, 2, \ldots, N_m) \tag{43}$$

where $\phi_k(\mathbf{X})$ term represents the time-independent velocity potential, which is only function of spatial coordinates. This potential satisfies the Laplace's equation at any position in the fluid domain as

$$\nabla^2\phi_k(\mathbf{X}) = 0 \tag{44}$$

For the fluid motion at the boundary, the velocity of the fluid and structure should be in equilibrium along the normal direction of the wetted surface. This kinematical boundary condition can be expressed as

$$\frac{\partial\phi_k(\mathbf{X})}{\partial n} = \bar{\mathbf{u}}(\mathbf{X}) \cdot \mathbf{n}(\mathbf{X}) \simeq \bar{\mathbf{v}}_k(\mathbf{X}) \cdot \mathbf{A}_3(\mathbf{X}) \tag{45}$$

where $\bar{\mathbf{u}}_k(\mathbf{X})$ vector corresponds to kth modal displacements at position $\mathbf{X}$ on the fluid-structure interaction boundary surface, the $\mathbf{n}(\mathbf{X})$ vector denotes the unit vector directed out of the fluid at position $\mathbf{X}$, and the partial derivative $\partial/\partial n$ signifies the derivative in this unit direction. We simplify this kinematic boundary condition by taking the advantage of thin shell assumption, $\mathbf{X} \simeq \mathbf{R}$. Therefore, the unit normal at the boundary surface is assumed to be equivalent to the $\mathbf{A}_3$ director of the mid-surface of the shell, and the $\bar{\mathbf{v}}_k$ vector represents the kth modal displacements at the mid-surface. One can readily attain this vector at any position over an isogeometric element domain e by utilizing the in-vacuo modal displacements at the control points and associated NURBS basis functions as

$$\bar{\mathbf{v}}_k(\mathbf{R}(\boldsymbol{\xi})) \equiv \bar{\mathbf{v}}_k(\boldsymbol{\xi}) = \sum_{i=1}^{n_{cp}} R_i^e(\boldsymbol{\xi})\bar{\mathbf{v}}_{k_i} \tag{46}$$

Additionally, the contribution of the free surface waves are neglected by assuming oscillations with relatively high frequency. Consequently, the free surface boundary condition is defined as $\phi_k = 0$, which is referred to as "infinite frequency limit condition". In this study, the free surface boundary condition is satisfied by applying the method of images, as explained in Ergin and Uğurlu [68]. Accordingly, the method of images (classical Neumann's case) fulfills this particular condition during the solution of velocity potential. The velocity potentials ϕ_k in the fluid domain can be calculated by using the boundary element method. Therefore, the boundary integral equation for ϕ_k potential can be written as

$$C(\mathbf{X}_S)\phi_k(\mathbf{X}_S) = \int\limits_{S_w+S_i} \left(G(\mathbf{X}_S,\mathbf{X}_F)\frac{\partial \phi_k(\mathbf{X}_F)}{\partial n} - \phi_k(\mathbf{X}_F)\frac{\partial G(\mathbf{X}_S,\mathbf{X}_F)}{\partial n} \right) dS \tag{47}$$

where $\mathbf{X}_S$ and $\mathbf{X}_F$ denotes the global Cartesian coordinates of the source and field points, respectively. Note that the integral in the right-hand-side of Eq. 47 should be calculated over the area of wet S_w and imaginary S_i surface of the domain of the interest. The wet surface (S_w) represents the total fluid-structure interaction area of the structure and the imaginary surface (S_i) can be effortlessly defined by mirroring the wet surface of structure with respect to the free surface plane of the fluid domain (see Fig. 4).

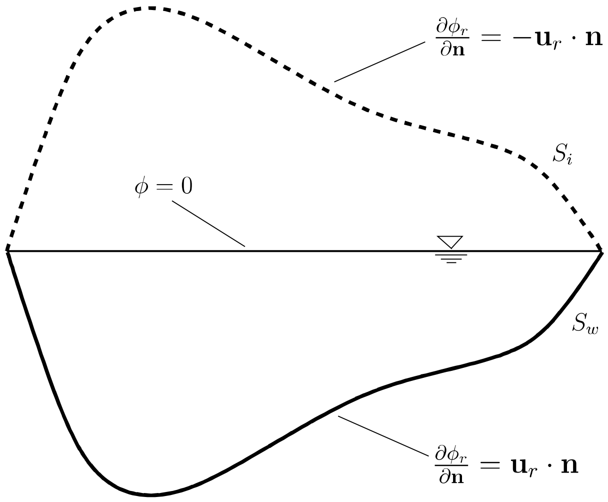

Figure 4: Wetted surface and its image.

Moreover, in Eq. 47, the solid (space) angles of the source locations can be defined as

$$C(\mathbf{X}_S) = \int\limits_{S_w+S_i} \frac{\partial G(\mathbf{X}_S, \mathbf{X}_F)}{\partial n}\, dS_F \tag{48}$$

Besides, the $G(\mathbf{X}_S, \mathbf{X}_F)$ denotes the fundamental solution of the Laplace's equation for which the basic Green's function can be selected by neglecting terms associated with wave mechanics as

$$G(\mathbf{X}_S, \mathbf{X}_F) = \frac{1}{\|\mathbf{X}_F - \mathbf{X}_S\|} \tag{49}$$

which satisfies the continuity condition and all boundary conditions everywhere in the fluid domain with the exception of evaluation point (e.g., when field and source locations coincide). The surface normal derivative of the Green's function at the field locations can be expressed as

$$\frac{\partial G(\mathbf{X}_S, \mathbf{X}_F)}{\partial n} = \nabla G(\mathbf{X}_S, \mathbf{X}_F) \cdot \mathbf{n}(\mathbf{X}_F) = \sum_{i=1}^{3} \left(\frac{\partial G(\mathbf{X}_S, \mathbf{X}_F)}{\partial x_i} \mathbf{A}_3(\mathbf{X}_F) \cdot \mathbf{e}_i \right) \tag{50}$$

where the derivatives of Green's function with respect to components of the global coordinate system can be calculated as

$$\frac{\partial G(\mathbf{X}_S, \mathbf{X}_F)}{\partial x_i} = -\frac{(\mathbf{X}_F - \mathbf{x}_S) \cdot \mathbf{e}_i}{\|\mathbf{X}_F - \mathbf{x}_S\|^3} \quad (i = 1, 2, 3) \tag{51}$$

Once the wetted and imaginary surfaces of the structure are discretized by NURBS basis functions, the same geometry functions can be utilized to approximate the velocity potentials (i.e., main unknowns) of boundary integral equation for its numerical solution. The geometrical discretization of the wet surface can be performed similar to the approach used in Eq. 26 as

$$\mathbf{X} = \mathbf{R}(\boldsymbol{\xi}) = \mathbf{N}^e \mathbf{P}^e \tag{52}$$

whereas the $\phi_k \equiv \phi_k(\boldsymbol{\xi})$ potential can be approximated over a boundary element surface as

$$\phi_k = \sum_{i=1}^{n_{cp}} R_i^e(\boldsymbol{\xi}) \phi_{k_i}^e = \begin{bmatrix} R_i^e(\boldsymbol{\xi}) & \cdots & R_{n_{cp}}^e(\boldsymbol{\xi}) \end{bmatrix} \begin{Bmatrix} \phi_{k_1}^e \\ \vdots \\ \phi_{k_{n_{cp}}} \end{Bmatrix} = \tilde{\mathbf{N}}^e \tilde{\boldsymbol{\Phi}}_k^e \tag{53}$$

where the $\phi^{e}_{k_i}$ $(i = 1, 2, \ldots, n_{cp})$ terms represent the source strengths at the ith control point of element $e = 1, 2, \ldots, n_{el}$ due to the kth vibration mode. For brevity, these unknown DOF and their associated non-zero NURBS basis functions are in the $\tilde{\boldsymbol{\Phi}}^{e}_{k}$ and $\tilde{\mathbf{N}}^{e}$ vectors, respectively. Substituting Eqs. 53 and 52 into Eq. 47 and applying the kinematic boundary condition, the surface integral equation for a given source location $\mathbf{X}_S$ can be cast in a vector form as

$$\tilde{C}(\mathbf{X}_S)\phi_k(\mathbf{X}_S) = \tilde{G}_k(\mathbf{X}_S) + \tilde{\mathbf{H}}(\mathbf{X}_S)\tilde{\boldsymbol{\Phi}}_k \tag{54}$$

with scalar terms obtained by summation of integral terms taken over the S^e area of NURBS element domain as

$$\tilde{C}(\mathbf{X}_S) = \sum_{e=1}^{n_{el}} \int_{S^e} \sum_{i=1}^{3} \left(\frac{(\mathbf{X} - \mathbf{x}_S) \cdot \mathbf{e}_i}{\|\mathbf{X} - \mathbf{x}_S\|^3} \mathbf{A}_3(\mathbf{X}) \cdot \mathbf{e}_i \right) dS^e \tag{55}$$

and

$$\tilde{G}_k(\mathbf{X}_S) = \sum_{e=1}^{n_{el}} \int_{S^e} \frac{\bar{\mathbf{v}}_k(\mathbf{X}) \cdot \mathbf{A}_3(\mathbf{X})}{\|\mathbf{X} - \mathbf{X}_S\|} \, dS^e \tag{56}$$

and vectorial terms obtained through the assembly of element contributions as

$$\tilde{\boldsymbol{\Phi}}_k = \bigcup_{e=1}^{n_{el}} \tilde{\boldsymbol{\Phi}}^{e}_{k}, \quad \tilde{\mathbf{H}}(\mathbf{X}_S) = \bigcup_{e=1}^{n_{el}} \tilde{\mathbf{H}}^{e}(\mathbf{X}_S) \tag{57}$$

where the $\tilde{\mathbf{H}}^e$ vector has the size of $1 \times n_{cp}$ and explicitly defined as

$$\tilde{\mathbf{H}}^{e}(\mathbf{X}_S) = \int_{S^e} \sum_{i=1}^{3} \left(\frac{\partial G(\mathbf{X}_S, \mathbf{X}}{\partial x_i} \mathbf{A}_3(\mathbf{X}) \cdot \mathbf{e}_i \right) \tilde{\mathbf{N}}^{e} \, dS^e \tag{58}$$

In Eq. 57, the $\tilde{\boldsymbol{\Phi}}_k$ and $\tilde{\mathbf{H}}$ vectors with the size of $N_{cp} \times 1$ and $1 \times N_{cp}$ contain all unknown source strengths and derivatives of the Green's function for the whole discretization, respectively. Once the Jacobian matrices are established for individual isogeometric elements, the inverse of Jacobians and their determinants can be utilized to compute the Cartesian derivatives $\partial G/\partial x_i$ given in Eq. 58 and perform the area integrals in Eqs. 55-58, respectively. The Gaussian quadrature is applied to perform the integrations numerically. Here, by following the strategy presented by Beer [69], a number of quadrature points is determined due to the distance between source and field points. In this study, the number of quadrature points are varied from 2 × 2 to 10 × 10 points. If the Eq. 54 is written for finite number of source locations and these positions are selected as being coincident with the position of control points, $S = 1, 2, \dots, N_{cp}$, then the velocity potentials $\phi_k(\mathbf{X}_S)$ become identical to the source strengths at the Sth control point. Therefore, the overall N_{cp} number of vectorial equations of the fluid domain can be cast in the following matrix-vector representation

$$\left(\begin{bmatrix} \tilde{C}(\mathbf{X}_1) & 0 & \cdots & 0 \\ & \tilde{C}(\mathbf{X}_2) & \cdots & \vdots \\ & & \ddots & 0 \\ \text{sym} & & & \tilde{C}(\mathbf{X}_{N_{cp}}) \end{bmatrix} + \begin{Bmatrix} \tilde{\mathbf{H}}(\mathbf{X}_1) \\ \tilde{\mathbf{H}}(\mathbf{X}_2) \\ \vdots \\ \tilde{\mathbf{H}}(\mathbf{X}_{N_{cp}}) \end{Bmatrix}\right) \tilde{\mathbf{\Phi}}_k = \begin{Bmatrix} \tilde{G}_k(\mathbf{X}_1) \\ \tilde{G}_k(\mathbf{X}_2) \\ \vdots \\ \tilde{G}_k(\mathbf{X}_{N_{cp}}) \end{Bmatrix} \Rightarrow \tilde{\mathbf{C}}\tilde{\mathbf{\Phi}}_k = \tilde{\mathbf{G}}_k \tag{59}$$

which can be solved to identify unknown source strengths $\tilde{\mathbf{\Phi}}_k$ of all control points utilized to define the whole NURBS discretization. Once the source strengths of control points are obtained, they can be interpolated as given in Eq. 53 to calculate the velocity potentials at any position in the fluid domain.

2.3.1. Wet Analysis – Calculation of wet frequencies and mode shapes

Neglecting the high-order terms in the Bernoulli's equation, the dynamic fluid pressure corresponding to the kth dry mode of the vibration can be expressed as

$$P_k(\mathbf{X}, t) = -\rho_s \dot{\mathbf{\Phi}}_k(\mathbf{X}, t) = \mathrm{Re}\{\phi_k(\mathbf{X})\omega^2 \bar{p}_k e^{i\omega t}\} \tag{60}$$

which can be integrated over the wet surface of the elastic structure to be able to calculate the generalized fluid-structure interaction forces as

$$F_{rk}(t) = \int\limits_{S_w} P_k \bar{\mathbf{v}}_r \cdot \mathbf{A}_3 \, dS = \left(\rho_f \int\limits_{S_w} \phi_k \bar{\mathbf{v}}_r \cdot \mathbf{A}_3 \, dS\right) \mathrm{Re}\{\omega^2 \bar{p}_k e^{i\omega t}\} = -A_{rk}\ddot{p}_k(t) \quad (r = 1, 2, \dots, N_m) \tag{61}$$

where A_{rk} represents the generalized added mass due to the coupled vibration modes of r and k, and F_{rk} is the corresponding inertial force, i.e., fluid-structure interaction force. For the sake of convenience with the matrix-vector definition, the Eq. 61 can be rewritten as

$$\mathbf{F} = -\mathbf{A}\ddot{\mathbf{p}}(t) = \omega^2 \mathbf{A}\bar{\mathbf{p}}e^{i\omega t} \tag{62}$$

where the $\mathbf{A}$ matrix has the size of $N_m \times N_m$ and contains the generalized added masses, and the $\mathbf{F}$ vector with the size of $N_m \times 1$ denotes the generalized fluid-structure force. While canceling the common exponential term, the fluid-structure forces can be set to the right-hand-side of natural vibration equations for an in vacuo structure (i.e., Eq. 39) as

$$\big(\mathbf{b} - \omega^2(\mathbf{a} + \mathbf{A})\big)\,\bar{\mathbf{p}} = 0 \tag{63}$$

which attains a classical form of an eigenvalue problem to evaluate the vibration modes and associated modal displacements of a structure partially in contact with fluid.

3. Experimental Modal Analysis

3.1. Equipment

Experimental modal testing requires several hardware components. The required basic equipments are identified as an excitation system to provide a known or controlled input force to the structure, a transducer that converts the accelerations or motions of the structure into an electrical signal, signal conditioning device, analyzer for executing signal processing and modal analysis software (see Fig. 5).

In this study, Bruel & Kjaer 8206-001 impact hammer was used for excitation. The impact hammer has a total voltage range of 445 N, with a typical voltage accuracy of 11.4 mV/N, and a total weight of 100 grams. The hammer is made of stainless steel and has a BNC type connection. Bruel & Kjaer 4507B Deltatron transducer was used as an accelerometer. Accuracy of the accelerometer is 9.63 $\mathrm{mV/ms^{-2}}$, frequency range is between 0.3 Hz–6 kHz, and the measurement range is +/- 71 g. The base material of the accelerometer is

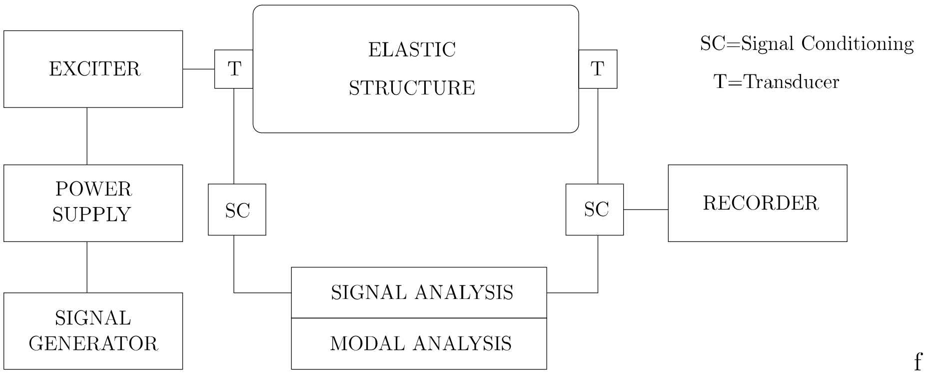

Figure 5: Diagram of experimental setup

made of titanium ATM grade 2, with a total weight of 4.8 grams. The analyzer used in this study is the Bruel & Kjaer 3560-B-040 PULSE 5-channel data acquisition system. The frequency range of the system is between 0–25.6 kHz. The system has five input and one output channels and also has a 24 bit analog digital converter and 24 bit data transfer capacity.

3.2. Experimental Setup

In this study, experimental modal analysis of a horizontal circular cylindrical shell partially filled with water was performed, and the natural frequencies and corresponding mode shapes of the structure were measured. A cylindrical shell of length $L = 1284$ mm, radius $r = 180$ mm, and thickness $h = 3$ mm is considered in this study (see Fig. 6). The structure is made of stainless steel with the following material characteristics: Young's modulus $E = 200$ GPa, Poisson's ratio $\nu = 0.29$ and mass density $\rho_s = 7900$ kg/m^3. The cylindrical shell is sealed at both ends, and it was experimentally investigated, respectively, in air and when partially or fully filled with water. The cylinder was attached to steel-made carrier by elastic springs of which rigidity were chosen to eliminate the natural modes of the carrier system. In the experiments in air, in order to accurately determine the mode shapes of the shell both in longitudinal and circumferencial directions, an appropriate number of excitation points has been chosen along the cylinder and around its circumference. Therefore, 11 points

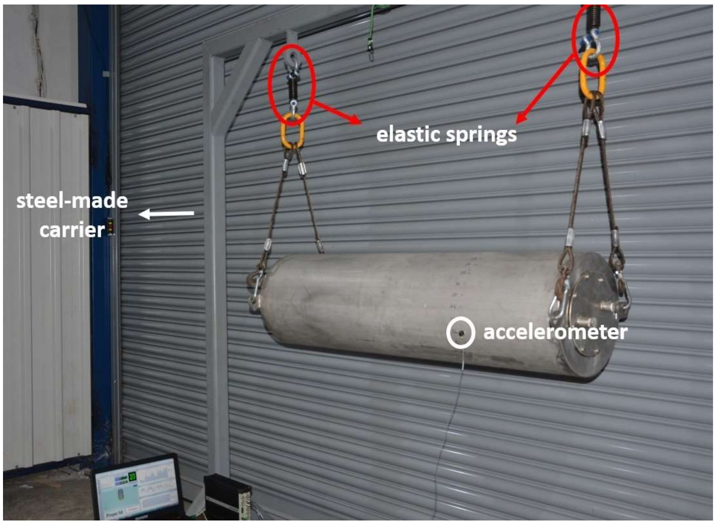

Figure 6: Experimental setup for modal analysis

along the length and 10 points around the circumference were selected for the experiments in air. In case of the cylindrical shell partially or fully filled with water, circumferential modes were measured at 30 equally-spaced excitation points chosen around the circumference at a distance of L/4 from one end. The experimental setup for the wet analysis is shown in Fig. 6.

In all the experiments, the standard modal testing procedures were applied, and the elastic structure was excited impulsively at the selected excitation points by the instrumented hammer. The accelerometer was attached at a specific fixed position during the tests (see Fig. 6). The frequency response functions (FRF) for each excitation is obtained by PULSE LabShop software.

4. Numerical Results and Comparison with Experiments

In this section, the vibration characteristics of the horizontal circular cylindrical shell partially filled with water are obtained by the proposed numerical framework. The numerical results are compared with those obtained by experiments to show the applicability of the numerical framework. The term $d/2r$ is used to denote the filling ratio, where d is the filling depth of fluid with a density

$\rho_f = 1000$ kg/m^3. As can be seen from Fig. 6, the cylindrical shell used in the experiments is sealed by steel plates at both ends. These end plates restrain the motion in radial direction and behave as simple supports at the ends of the cylindrical shell. Therefore, in the numerical simulations, instead of modeling end plates, simple support boundary condition is applied for both ends.

In the dry part of the numerical framework, the in-vacuo dynamic characteristics were obtained by solving the free vibration problem formulated based on isogeometric finite element method (IGAFEM). The cylindrical shell was represented by a 2nd-order NURBS patch. Importantly, the computational domain was modeled as a half cylinder to take the advantage of symmetry of the structure. As reported in Ergin and Temarel [38], the results occur in pairs when the problem is solved by using the whole geometry (i.e. cylinder) in the simulations. In this case, for each natural frequency, a pair of mode shapes-symmetric and antisymmetric-is obtained. Indeed, the obtained pairs have the same modal shapes (and the same frequencies) but different orientations: one of them becomes symmetric while the other one is antisymmetric with respect to a plane. Therefore, in this study, the following procedure is adopted in the dry analysis of the horizontal cylindrical shell: (1) Antisymmetric mode shapes are obtained by solving the eigenvalue problem by modeling the computational domain as a half cylinder and applying appropriate antisymmetry boundary conditions; (2) the symmetric mode shapes are generated accordingly by using the antisymmetric mode shapes (i.e. antisymmetric modal shapes are appropriately rotated); (3) the orthogonality condition is checked for the generated modes. Here, it must be remarked that the symmetric boundary conditions cannot be applied as the IGAFEM procedure is purely displacement-based, i.e. rotation-free formulation does not allow us to apply symmetric boundary conditions. Moreover, by modeling the structure as a half cylinder, the symmetry plane is automatically defined in the numerical simulations.

For the dry analysis, a convergence study was carried out to assess the accuracy of the calculated dry natural frequencies. The numerical results obtained via isogeometric finite element method (IGAFEM) are compared with those obtained by ANSYS and experiments. The half cylinder was modeled with four different idealizations (i.e. NURBS patches). In the first test study, the NURBS patch was discretized with 1800 elements-30 elements along circumference and 60 elements along length. Then, the number of elements was increased to 2592 (36 elements along circumference and 72 elements along length) and 3528 (42 elements along circumference and 84 elements along length), respectively, in the second and third idealizations. Finally, in the fourth test study, the NURBS patch was discretized with 4608 elements (48 elements along circumference and 96 elements along length). In the ANSYS simulation, the computational domain was modeled as a cylinder with 9216 elements. The dry natural frequencies obtained for each idealization can be seen in Table 1, for the first twelve modes (i.e., for the first six mode pairs). Here, the dry mode numbers (m, n) of the cylindrical structure are identified with the number of standing waves around the circumference (n), and the number of half-waves along the length of the shell (m). It must also be realized that the fundamental dry natural frequency does not correspond to the mode shape with the lowest number of waves around the circumference $(n = 2)$. The order of modes depends on the geometrical characteristics of the cylindrical shell.

As presented in Table 1, the converged dry natural frequencies are validated with experimental results. Moreover, IGAFEM results compare very well with those obtained by ANSYS. Here, in the ANSYS simulation, the problem was solved by discretizing the whole geometry. In this way, the validity of the adopted numerical strategy (i.e. applying antisymmetric boundary conditions to a half cylinder in IGAFEM simulations) is shown. Furthermore, the mode shapes obtained by experiments and numerical simulations (both ANSYS and IGAFEM) are presented in Fig. 7, for the first six mode pairs, namely, $(1, 2)$, $(1, 3)$, $(1, 4)$, $(2, 3)$, $(2, 4)$, and $(1, 5)$. The predicted mode shapes using IGAFEM compare very well with the corresponding experimentally measured mode shapes and with those obtained by ANSYS.

In the wet part of the study, the proposed IGABEM procedure is applied for obtaining the wet dynamic characteristics, i.e. wet natural frequencies and

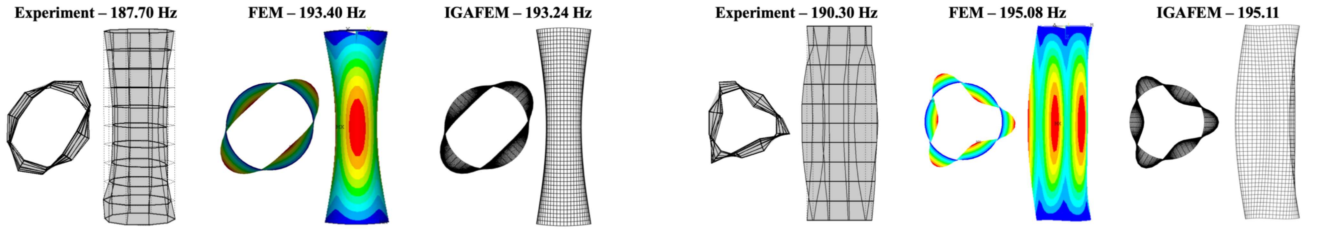

(a) Mode (1,2)

(b) Mode (1,3)

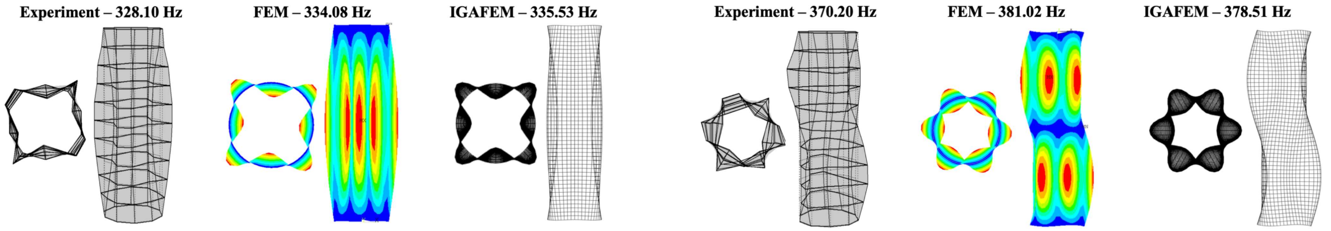

(c) Mode (1,4)

(d) Mode (2,3)

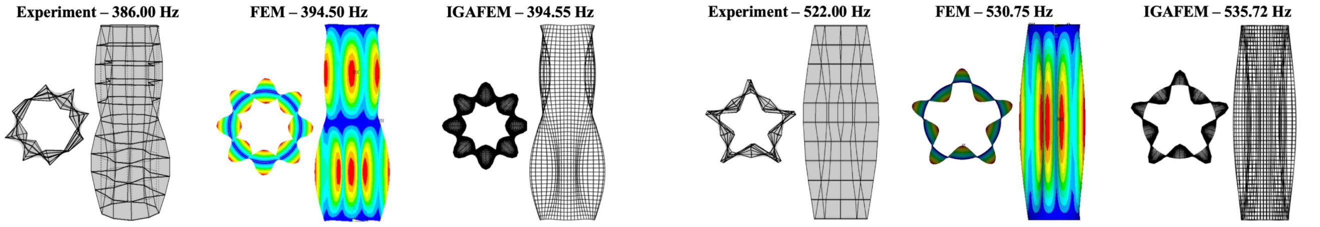

(e) Mode (2,4)

(f) Mode (1,5)

Figure 7: Dry mode shapes obtained by IGAFEM, experiments and FEM (ANSYS®)

Mode No	**IGAFEM**				**FEM (ANSYS®)**	**Experiment**
(m,n)	1800 El.	2592 El.	3528 El.	4608 El.	9216 El.	**Measurements**
(1,2)	193.49	193.34	193.27	193.24	193.35	187.70
(1,2)	193.49	193.34	193.27	193.24	193.35	-
(1,3)	197.33	196.00	195.41	195.11	194.58	190.30
(1,3)	197.33	196.00	195.41	195.11	194.58	-
(1,4)	340.97	337.77	336.30	335.53	333.03	328.10
(1,4)	340.97	337.77	336.30	335.53	333.03	-
(2,3)	379.65	378.98	378.67	378.51	380.76	370.20
(2,3)	379.65	378.98	378.67	378.51	380.76	-
(2,4)	399.16	396.46	395.21	394.55	394.48	386.00
(2,4)	399.16	396.46	395.21	394.55	394.48	-
(1,5)	546.56	540.26	537.31	535.72	530.75	521.00
(1,5)	546.56	540.26	537.31	535.72	530.75	-

Table 1: Convergence of in-vacuo natural frequencies (Hz) and comparison with FEM and experimental results (the 9216 elements of FEM solution refer to the whole geometry while the 4608 elements of IGAFEM solution refer to the half of the geometry).

corresponding mode shapes, for the horizontal cylindrical circular shell under study. In order to test the convergence of the hydrodynamic predictions, various numbers of boundary elements (panels) were distributed over the wetted surface. The numerical simulations were carried out for four different filling ratios, namely, $d/2r = 0.25$, 0.50, 0.75, and 1.00. Here, the idealizations are identified by the number of hydrodynamic panels distributed around the circumference and along the shell, respectively. In the first idealizations, the number of total panels distributed over the wetted surfaces was 180, 270, 360, and 540 for the filling ratios 0.25, 0.50, 0.75, and 1.00, respectively. For each filling ratio, the number of panels was 15 along the length of the cylinder while the number of panels was 12, 18, 24, and 36 around the circumference, respectively, for $d/2r =$ 0.25, 0.50, 0.75, and 1.00. Subsequently, the number of total panels distributed over the wetted surfaces was increased to 320, 480, 640, and 960 for the second idealization and 500, 750, 1000, and 1500 for the third idealization, respectively, for the filling ratios $d/2r = 0.25$, 0.50, 0.75, and 1.00. In the second and the

Mode No	180 Panels	320 Panels	500 Panels	720 Panels
1	128.30	125.76	124.03	123.57
2	129.35	127.45	126.14	126.02
3	180.26	178.95	178.25	177.81
4	192.08	191.77	191.57	191.43
5	259.45	252.71	249.47	247.65
6	273.53	265.68	261.70	259.40

(a) $d/2r = 0.25$

Mode No	270 Panels	480 Panels	750 Panels	1080 Panels
1	110.44	109.11	108.49	108.15
2	112.85	111.22	110.45	110.03
3	161.20	159.22	158.26	157.72
4	166.35	165.16	164.56	164.22
5	239.51	233.48	230.65	229.10
6	243.26	236.57	233.42	231.69

(b) $d/2r = 0.50$

Mode No	360 Panels	640 Panels	1000 Panels	1440 Panels
1	102.62	101.33	100.72	100.39
2	104.46	103.04	102.38	102.01
3	138.71	137.11	136.35	135.93
4	142.23	140.21	139.24	138.71
5	225.31	219.40	216.65	215.15
6	228.37	222.22	219.34	217.76

(c) $d/2r = 0.75$

Mode No	540 Panels	960 Panels	1500 Panels	2160 Panels
1	96.39	95.41	94.96	94.72
2	96.54	95.62	95.19	94.95
3	108.93	106.96	106.05	105.56
4	109.37	107.53	106.66	106.18
5	207.56	201.89	199.26	197.82
6	208.63	203.41	200.91	199.53

(d) $d/2r = 1.00$

Table 2: Convergence of wet natural frequencies (Hz) for filling ratios $d/2r = 0.25$, 0.50, 0.75 and 1.00.

third idealizations, the number of panels along the length of the wetted surfaces was 20 and 25, respectively. In the last group of simulations, the number total panels was increased to 720, 1080, 1440, and 2160 for filling ratios $d/2r = 0.25$, 0.50, 0.75, and 1.00, respectively. The number of panels along the length was 30 for each filling ratio while the number of panels along the circumference was 36, 48, 60, and 72, for filling ratios $d/2r = 0.25$, 0.50, 0.75, and 1.00, respectively. Also, an additional convergence study was carried out to determine the number of in-vacuo modes needed for the wet converged results. As a result of this additional analysis, 48 in-vacuo modes (24 in-vacuo mode pairs) were included in the calculations.

Mode	IGAFEM-IGABEM Results Filling Ratio ($d/2r$)				FEM (ANSYS®) Filling Ratio ($d/2r$)				Experiment Filling Ratio ($d/2r$)			
	0.25	0.5	0.75	1.0	0.25	0.5	0.75	1.0	0.25	0.5	0.75	1.0
1	123.57	108.15	100.39	94.72	129.28	109.50	102.88	97.20	128.10	111.10	99.70	93.70
2	126.02	110.03	102.01	94.95	131.65	111.40	105.83	97.20	130.80	114.00	104.20	94.60
3	177.81	157.72	135.93	105.56	182.53	158.70	135.34	108.20	179.20	159.20	137.10	105.50
4	191.43	164.22	138.71	106.18	191.56	159.90	138.46	108.20	186.20	164.90	143.00	106.50
5	247.65	229.10	215.15	197.82	261.10	235.40	225.62	195.20	256.40	228.40	222.10	195.20
6	259.40	231.69	217.76	199.53	266.88	238.90	227.76	195.20	262.40	230.90	224.90	196.40

Table 3: Comparison of wet frequencies (Hz) obtained by both numerical simulations and experiments

The convergence of wet natural frequencies are presented in Table 2, for four different filling ratios, $d/2r = 0.25$, 0.50, 0.75, and 1.00, respectively. As shown in Table 2, the results show monotonic convergence, and it is clear that the differences between the third and fourth groups of calculations are reasonably small for each filling ratio. Therefore, the last group of idealizations (720, 1080, 1440, and 2160 panels) are used in the computation of wet dynamic characteristics.

The calculated wet natural frequencies are compared with those obtained by ANSYS and experiments in Table 3 for the first six wet modes. As presented in Table 3, the predicted wet natural frequencies compare very well with the experimental measurements and FEM results. The differences are in the range of 0.78%-3.66% for $d/2r = 0.25$, 0.3%-3.48% for $d/2r = 0.50$, 0.69%-3.17% for $d/2r = 0.75$, and 0.06%-1.59% for $d/2r = 1.00$. The maximum difference (3.66%) was obtained for the second mode of the filling ratio $d/2r = 0.25$. As expected, wet natural frequencies are lower than their dry counterparts due to the presence of fluid. In ANSYS, the cylindrical shell was discretized with four-node quadrilateral SHELL181 elements, and the fluid was modeled with FLUID30 elements. The density and sonic velocity of fluid are taken as 1000 kg/m^3 and 1507 m/s, respectively. As the structure vibrates in high frequency region, the infinite frequency limit condition is imposed on the free surface of contained fluid. The circular sealings at the ends of the shell are assumed to be rigid, and therefore, the fluid actions are omitted over the ends of the cylinder.

Additionally, the wet mode shapes obtained by the isogemetric FE-BE pro-

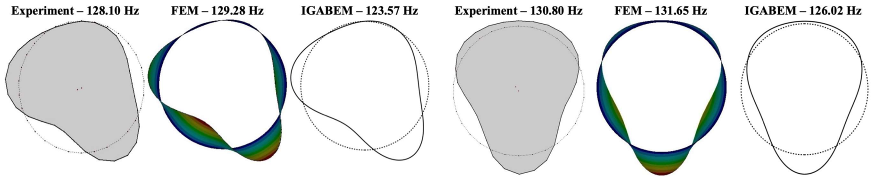

(a) 1st Wet Mode (b) 2nd Wet Mode

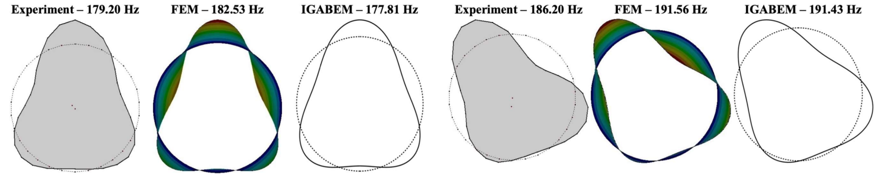

(c) 3rd Wet Mode (d) 4th Wet Mode

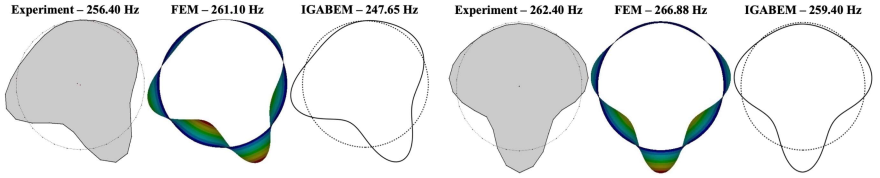

(e) 5th Wet Mode (f) 6th Wet Mode

Figure 8: Calculated and measured wet mode shapes for filling ratio $d/2r = 0.25$

cedure are presented in Figs. 8, 9, 10 and 11 for the filling ratios $d/2r = 0.25$, 0.50, 0.75 and 1.00, respectively. For each filling ratio, the first six wet mode shapes are presented and compared with those obtained by ANSYS and experiments. As can be seen from Figs. 8, 9, 10, in case of that the horizontal cylindrical circular shell is partially-filled, the mode shapes are quite similar to each other but considerably different from those obtained in air/vacuo. On the other hand, for the fully-filled case ($d/2r = 1.00$), the calculated wet mode shapes are similar to those measured in air but with lower natural frequency values (see Fig. 11). It should also be said that the calculated mode shapes obtained by the proposed isogeometric FE-BE method compare perfectly well to the mode shapes obtained by ANSYS and experiments.

Furthermore, the calculated generalized added mass values are presented for

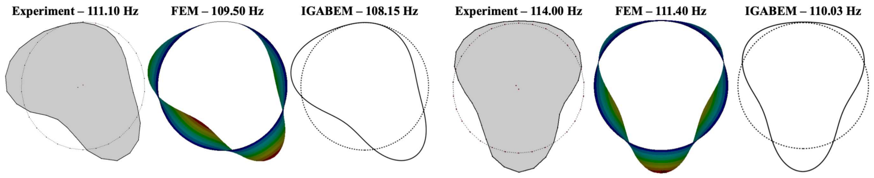

(a) 1st Wet Mode (b) 2nd Wet Mode

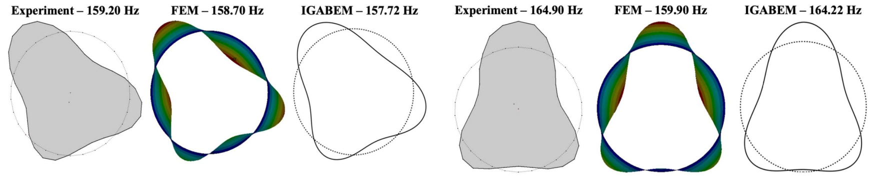

(c) 3rd Wet Mode (d) 4th Wet Mode

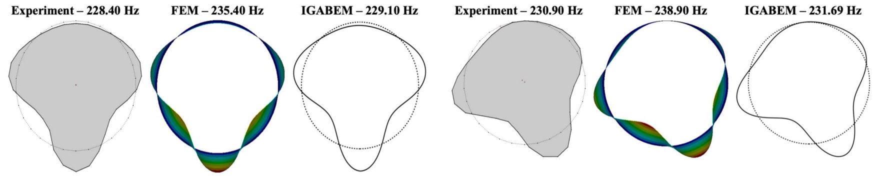

(e) 5th Wet Mode (f) 6th Wet Mode

Figure 9: Calculated and measured wet mode shapes for filling ratio $d/2r = 0.50$

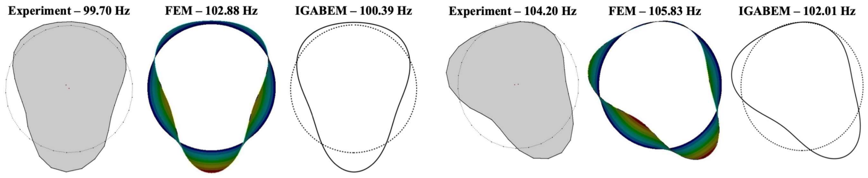

(a) 1st Wet Mode (b) 2nd Wet Mode

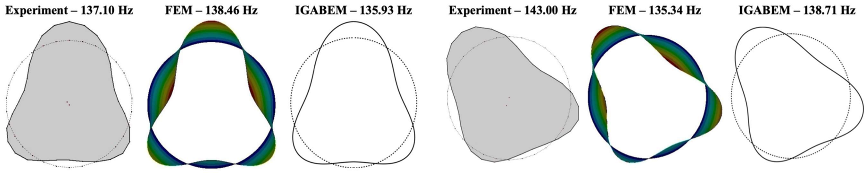

(c) 3rd Wet Mode (d) 4th Wet Mode

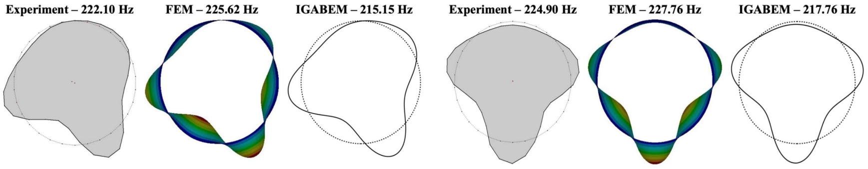

(e) 5th Wet Mode (f) 6th Wet Mode

Figure 10: Calculated and measured wet mode shapes for filling ratio $d/2r = 0.75$

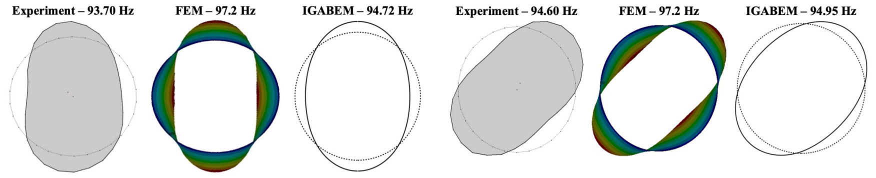

Experiment – 93.70 Hz FEM – 97.2 Hz IGABEM – 94.72 Hz

Experiment – 94.60 Hz FEM – 97.2 Hz IGABEM – 94.95 Hz

(a) 1st Wet Mode (b) 2nd Wet Mode

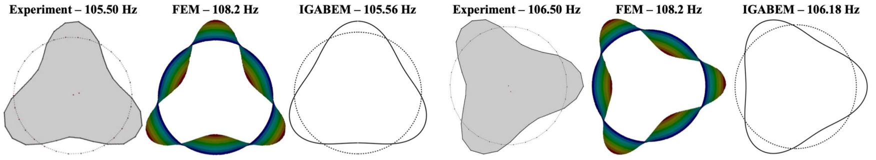

Experiment – 105.50 Hz FEM – 108.2 Hz IGABEM – 105.56 Hz

Experiment – 106.50 Hz FEM – 108.2 Hz IGABEM – 106.18 Hz

(c) 3rd Wet Mode (d) 4th Wet Mode

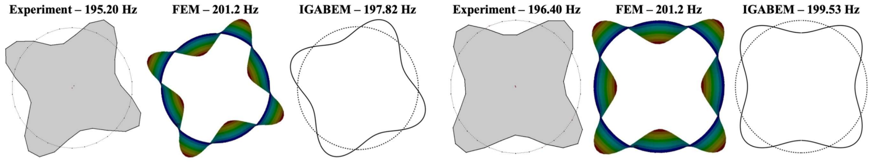

Experiment – 195.20 Hz FEM – 201.2 Hz IGABEM – 197.82 Hz

Experiment – 196.40 Hz FEM – 201.2 Hz IGABEM – 199.53 Hz

(e) 5th Wet Mode (f) 6th Wet Mode

Figure 11: Calculated and measured wet mode shapes for filling ratio $d/2r = 1.00$

Mode	1(A)	2(S)	3(A)	4(S)	5(A)	6(S)	7(A)	8(S)	9(A)	10(S)	11(A)	12(S)
1(A)	0.70	0.00	0.69	0.00	-0.42	0.00	0.00	0.00	0.00	0.00	-0.09	0.01
2(S)	0.00	0.94	0.00	0.57	0.00	-0.21	0.00	0.00	0.00	0.00	0.00	0.01
3(A)	0.69	0.00	0.72	0.00	-0.49	0.00	0.00	0.00	0.00	0.00	-0.19	0.01
4(S)	0.00	0.56	0.00	0.54	0.00	-0.41	0.00	0.00	0.00	0.00	0.00	-0.22
5(A)	-0.41	0.00	-0.49	0.00	0.43	0.00	0.00	0.00	0.00	0.00	0.28	-0.01
6(S)	0.00	-0.20	0.00	-0.40	0.00	0.47	0.00	0.00	0.00	0.00	0.00	0.36
7(A)	0.00	0.00	0.00	0.00	0.00	0.00	0.67	0.00	-0.48	-0.01	0.00	0.00
8(S)	0.00	0.00	0.00	0.00	0.00	0.00	0.00	0.48	0.00	-0.39	0.00	0.00
9(A)	0.00	0.00	0.00	0.00	0.00	0.00	-0.47	0.00	0.42	0.00	0.00	0.00
10(S)	0.00	0.00	0.00	0.00	0.00	0.00	-0.01	-0.39	0.00	0.45	0.00	0.00
11(A)	-0.08	0.00	-0.18	0.00	0.28	0.00	0.00	0.00	0.00	0.00	0.31	0.00
12(S)	0.01	0.02	0.01	-0.22	-0.01	0.36	0.00	0.00	0.00	0.00	0.00	0.36

(a) $d/2r = 0.25$

Mode	1(A)	2(S)	3(A)	4(S)	5(A)	6(S)	7(A)	8(S)	9(A)	10(S)	11(A)	12(S)
1(A)	1.57	0.00	0.85	0.00	0.00	0.00	0.00	0.00	0.00	0.00	0.24	0.03
2(S)	0.00	1.22	0.00	0.86	0.00	-0.17	0.00	0.00	0.00	0.00	0.00	0.22
3(A)	0.85	0.00	1.02	0.00	-0.67	0.00	0.00	0.00	0.00	0.00	-0.10	0.01
4(S)	0.00	0.86	0.00	1.19	0.00	-0.65	0.00	0.00	0.00	0.00	0.00	0.00
5(A)	0.00	0.00	-0.67	0.00	0.93	0.00	0.00	0.00	0.00	0.00	0.54	0.01
6(S)	0.00	-0.17	0.00	-0.65	0.00	0.81	0.00	0.00	0.00	0.00	0.00	0.51
7(A)	0.00	0.00	0.00	0.00	0.00	0.00	0.99	0.00	-0.69	-0.01	0.00	0.00
8(S)	0.00	0.00	0.00	0.00	0.00	0.00	0.00	1.17	0.01	-0.66	0.00	0.00
9(A)	0.00	0.00	0.00	0.00	0.00	0.00	-0.69	0.01	0.94	0.00	0.00	0.00
10(S)	0.00	0.00	0.00	0.00	0.00	0.00	-0.01	-0.66	0.00	0.81	0.00	0.00
11(A)	0.24	0.00	-0.10	0.00	0.54	0.00	0.00	0.00	0.00	0.00	0.69	0.01
12(S)	0.03	0.22	0.01	0.00	0.01	0.51	0.00	0.00	0.00	0.00	0.01	0.72

(b) $d/2r = 0.50$

Mode	1(A)	2(S)	3(A)	4(S)	5(A)	6(S)	7(A)	8(S)	9(A)	10(S)	11(A)	12(S)
1(A)	1.83	0.00	0.80	0.00	0.17	0.00	0.00	0.00	0.00	0.00	-0.16	-0.04
2(S)	0.00	1.96	0.00	0.90	0.00	0.31	0.00	0.00	0.00	0.00	0.00	-0.09
3(A)	0.80	0.00	1.59	0.00	-0.62	0.00	0.00	0.00	0.00	0.00	-0.22	0.01
4(S)	0.00	0.89	0.00	1.44	0.00	-0.66	0.00	0.00	0.00	0.00	0.00	-0.19
5(A)	0.17	0.00	-0.62	0.00	1.18	0.00	0.00	0.00	0.00	0.00	-0.54	-0.01
6(S)	0.00	0.31	0.00	-0.65	0.00	1.21	0.00	0.00	0.00	0.00	0.00	-0.46
7(A)	0.00	0.00	0.00	0.00	0.00	0.00	1.57	0.00	-0.64	-0.01	0.00	0.00
8(S)	0.00	0.00	0.00	0.00	0.00	0.00	0.00	1.40	0.01	-0.68	0.00	0.00
9(A)	0.00	0.00	0.00	0.00	0.00	0.00	-0.64	0.01	1.19	0.00	0.00	0.00
10(S)	0.00	0.00	0.00	0.00	0.00	0.00	-0.01	-0.67	0.00	1.21	0.00	0.00
11(A)	-0.16	0.00	-0.22	0.00	-0.54	0.00	0.00	0.00	0.00	0.00	0.95	-0.01
12(S)	-0.04	-0.09	0.01	-0.19	-0.01	-0.46	0.00	0.00	0.00	0.00	-0.01	0.96

(c) $d/2r = 0.75$

Mode	1(A)	2(S)	3(A)	4(S)	5(A)	6(S)	7(A)	8(S)	9(A)	10(S)	11(A)	12(S)
1(A)	3.16	0.00	0.00	0.00	0.00	0.00	0.00	0.00	0.00	0.00	0.00	0.00
2(S)	0.00	3.14	0.00	0.00	0.00	0.00	0.00	0.00	0.00	0.00	0.00	0.00
3(A)	0.00	0.00	2.42	0.00	0.00	0.00	0.00	0.00	0.00	0.00	0.00	0.00
4(S)	0.00	0.00	0.00	2.38	0.00	0.00	0.00	0.00	0.00	0.00	0.00	0.00
5(A)	0.00	0.00	0.00	0.00	1.88	0.00	0.00	0.00	0.00	0.00	0.00	0.00
6(S)	0.00	0.00	0.00	0.00	0.00	1.83	0.00	0.00	0.00	0.00	0.00	0.00
7(A)	0.00	0.00	0.00	0.00	0.00	0.00	2.38	0.00	0.00	0.00	0.00	0.00
8(S)	0.00	0.00	0.00	0.00	0.00	0.00	0.00	2.34	0.00	0.00	0.00	0.00
9(A)	0.00	0.00	0.00	0.00	0.00	0.00	0.00	0.00	1.89	0.00	0.00	0.00
10(S)	0.00	0.00	0.00	0.00	0.00	0.00	0.00	0.00	0.00	1.84	0.00	0.00
11(A)	0.00	0.00	0.00	0.00	0.00	0.00	0.00	0.00	0.00	0.00	3.34	0.00
12(S)	0.00	0.00	0.00	0.00	0.00	0.00	0.00	0.00	0.00	0.00	0.00	3.34

(d) $d/2r = 1.00$

Table 4: Generalized added mass coefficients (kg m^2) of cylindrical shell for filling ratios $d/2r = 0.25, 0.50, 0.75$ and 1.00 (A: Asymmetric Mode, S: Symmetric Mode).

the first 12 modes (first 6 mode pairs) in Table 4 for four different filling ratios, $d/2r = 0.25$, 0.50, 0.75 and 1.00, respectively. These values correspond to a generalized structural mass of 1 $\mathrm{kg\,m^2}$. As expected, the generalized added mass values increase with increasing filling ratios, due to increased wetted surface area. It can be observed that the diagonal terms of the generalized added mass matrices are significantly higher compared to the off-diagonal terms. Here, the off-diagonal terms represent the hydrodynamic coupling between the dry modes. It is also clear that hydrodynamic coupling between symmetric and antisymmetric modes is negligibly small. Importantly, as can be seen from Table 4d, when the cylindrical shell is fully-filled, hydrodynamic coupling between modes is negligibly small. Therefore, hydrodynamic coupling becomes more important for partially-filled cases (see Tables 4a, 4b, and 4c). Ergin and Temarel [38] reported that some symmetric and antisymmetric modes may have coupling as mode shapes obtained by FEM analysis is not perfectly symmetric or antisymmetric with respect to the plane of symmetry of the fluid-coupled system. In other words, the plane of symmetry of both the fluid-free and fluid-coupled analyses must be the same. However, as the cylindrical shell in vacuo has infinite number of symmetry planes when the whole cylinder is considered in the dry analysis, it is not guaranteed that the FEM results are symmetrical about the symmetry plane of the fluid-coupled system. One must assign a symmetry plane to the fluid-free system (dry structure), which is quite challenging, and this requires rotation of mode shapes accordingly to the symmetry plane assigned. In this study, this issue is eliminated by following the previously mentioned IGAFEM procedure. In the dry analysis, the problem was solved by modeling the cylindrical shell as a half cylinder, and therefore, the dry mode shapes were obtained perfectly symmetric or antisymmetric with respect to the plane of symmetry of the fluid-filled system.

5. Conclusions

In this study, the hydroelastic vibration characteristics (i.e. natural frequencies and associated mode shapes) of a partially filled cylindrical shell were investigated by an isogeometric FE-BE method. In order to show the applicability of the proposed method, the numerical predictions are compared and validated with those obtained from the experiments.

In the dry analysis, the in-vacuo dynamic characteristics of the cylindrical shell were obtained by the isogeometric finite element method (IGAFEM) based on a linear Kirchhoff-Love shell formulation. The dry natural frequencies and associated mode shapes were obtained with a discretization of 2nd-order NURBS patch with 4608 elements (48 elements around circumference and 96 elements along the shell). From the results presented (see Table 1 and Fig. 7), the IGAFEM calculations show a good agreement with standard FEM results and experimental measurements. Importantly, as explained in Section 4 in detail, to have the same plane of symmetry both in the fluid-free and fluid-coupled systems, the dynamic characteristics of the cylindrical shell was obtained by modeling the structure as a half cylinder in IGAFEM simulations.

In the wet analysis, 48 in-vacuo modes (24 symmetric and 24 antisymmetric) were included to investigate the wet dynamic characteristics of the cylindrical shell for four different filling ratios. For the hydrodynamic calculations, the converged wet dynamic characteristics were obtained with discretizations of 720, 1080, 1440, and 2160 hydrodynamic panels, respectively, for filling ratios $d/2r = 0.25, 0.50, 0.75$, and 1.00 (see Table 2). As can be seen from the presented results (see Table 3), numerical calculations (both FEM and IGABEM) and experimental measurements are in an excellent agreement with the differences being in an acceptable range. The calculated wet natural frequencies significantly decrease with increasing filling ratios. In other words, the generalized added mass terms increase as a result of increase in wetted surface area, causing decrease in wet natural frequencies. In addition, it is observed that diagonal generalized added mass terms are considerably higher than off-diagonal ones, and the hydrodynamic coupling between symmetric and antisymmetric modes is negligibly small (see Table 4).

The present work has demonstrated the versatility of the proposed isogeometric FE-BE framework for the hydroelastic vibration analysis of high-frequency structures. In a further study, in order to account the free surface effects, extension of the existing code is currently under development to implement isogeometric FE-BE method in conjunction with the free surface Green's function.

Acknowledgements

This work was funded by Istanbul Technical University under ITU-BAP Project No 42058.

References

[1] S. Alessandroni, U. Andreaus, F. dell'Isola, M. Porfiri, A passive electric controller for multimodal vibrations of thin plates, Computers & structures 83 (15-16) (2005) 1236–1250.

[2] A. M. Bersani, A. Della Corte, G. Piccardo, N. L. Rizzi, An explicit solution for the dynamics of a taut string of finite length carrying a traveling mass: the subsonic case, Zeitschrift für angewandte Mathematik und Physik 67 (4) (2016) 108.

[3] A.-e.-n. N. Abd-alla, F. Alshaikh, D. Del Vescovo, M. Spagnuolo, Plane waves and eigenfrequency study in a transversely isotropic magneto-thermoelastic medium under the effect of a constant angular velocity, Journal of Thermal Stresses 40 (9) (2017) 1079–1092.

[4] E. Barchiesi, M. Laudato, F. Di Cosmo, Wave dispersion in non-linear pantographic beams, Mechanics Research Communications 94 (2018) 128–132.

[5] A. Cazzani, N. L. Rizzi, F. Stochino, E. Turco, Modal analysis of laminates by a mixed assumed-strain finite element model, Mathematics and Mechanics of Solids 23 (1) (2018) 99–119.

[6] I. Giorgio, D. Del Vescovo, Non-linear lumped-parameter modeling of planar multi-link manipulators with highly flexible arms, Robotics 7 (4) (2018) 60.

[7] I. Giorgio, D. Del Vescovo, Energy-based trajectory tracking and vibration control for multilink highly flexible manipulators, Mathematics and Mechanics of Complex Systems 7 (2) (2019) 159–174.

[8] D. Baroudi, I. Giorgio, A. Battista, E. Turco, L. A. Igumnov, Nonlinear dynamics of uniformly loaded Elastica: Experimental and numerical evidence of motion around curled stable equilibrium configurations, ZAMM-Journal of Applied Mathematics and Mechanics/Zeitschrift für Angewandte Mathematik und Mechanik (2019) e201800121.

[9] V. Eremeyev, Strongly anisotropic surface elasticity and antiplane surface waves, Philosophical Transactions of the Royal Society A (2019) 1–14.

[10] G. Warburton, Vibration of a cylindrical shell in an acoustic medium, Journal of Mechanical Engineering Science 3 (1) (1961) 69–79.

[11] U. S. Lindholm, D. D. Kana, W.-H. Chu, H. N. Abramson, Elastic vibration characteristics of cantilever plates in water, Journal of Ship Research 9 (1965) 11–22.

[12] G. Zhang, T. Li, X. Zhu, J. Yang, Y. Miao, Free and forced vibration characteristics of submerged finite elliptic cylindrical shell, Ocean Engineering 129 (2017) 92–106.

[13] P. Wang, T. Li, X. Zhu, Free flexural vibration of a cylindrical shell horizontally immersed in shallow water using the wave propagation approach, Ocean Engineering 142 (2017) 280–291.

[14] M. Ji, K. Inaba, F. Triawan, Vibration characteristics of cylindrical shells filled with fluid based on first-order shell theory, Journal of Fluids and Structures 85 (2019) 275–291.

[15] X. Zhang, Frequency analysis of submerged cylindrical shells with the wave propagation approach, International Journal of Mechanical Sciences 44 (7) (2002) 1259–1273.

[16] K.-H. Jeong, S.-C. Lee, Fourier series expansion method for free vibration analysis of either a partially liquid-filled or a partially liquid-surrounded circular cylindrical shell, Computers & structures 58 (5) (1996) 937–946.

[17] K.-H. Jeong, Dynamics of a concentrically or eccentrically submerged circular cylindrical shell in a fluid-filled container, Journal of Sound and vibration 224 (4) (1999) 709–732.

[18] T. I. Thinh, M. C. Nguyen, Dynamic stiffness method for free vibration of composite cylindrical shells containing fluid, Applied Mathematical Modelling 40 (21-22) (2016) 9286–9301.

[19] M. N. Izyan, Z. Aziz, K. Viswanathan, Free vibration of anti-symmetric angle-ply layered circular cylindrical shells filled with quiescent fluid under first order shear deformation theory, Composite Structures 193 (2018) 189–197.

[20] A. Ergin, An approximate method for the free vibration analysis of partially filled and submerged, horizontal cylindrical shells, Journal of Sound and Vibration 207 (5) (1997) 761–767.

[21] M. Amabili, Vibrations of circular tubes and shells filled and partially immersed in dense fluids, Journal of Sound and Vibration 221 (4) (1999) 567–585.

[22] E. Askari, K.-H. Jeong, Hydroelastic vibration of a cantilever cylindrical shell partially submerged in a liquid, Ocean Engineering 37 (11-12) (2010) 1027–1035.

[23] M. Chiba, N. Yamaki, J. Tani, Free vibration of a clamped-free circular cylindrical shell partially filled with liquid – part II: Numerical results, Thin-Walled Structures 2 (4) (1984) 307–324.

[24] M. Amabili, Free vibration of partially filled, horizontal cylindrical shells, Journal of Sound and Vibration 191 (5) (1996) 757–780.

[25] M. Amabili, Flexural vibration of cylindrical shells partially coupled with external and internal fluids, Journal of Vibration and acoustics 119 (3) (1997) 476–484.

[26] P. Goncalves, N. Ramos, Free vibration analysis of cylindrical tanks partially filled with liquid, Journal of Sound and Vibration 195 (3) (1996) 429–444.

[27] C.-J. Liao, W.-K. Jiang, H. Duan, Y. Wang, Vibration and sound radiation from submerged finite cylindrical shells reinforced with axially periodic stiffeners, Journal of Vibration and Control 17 (10) (2011) 1472–1480.

[28] B. Laulagnet, J. Guyader, Sound radiation from finite cylindrical coated shells, by means of asymptotic expansion of three-dimensional equations for coating, The Journal of the Acoustical Society of America 96 (1) (1994) 277–286.

[29] M. Chiba, H. Magata, Influence of liquid sloshing on dynamics of flexible space structures, Journal of Sound and Vibration 401 (2017) 1–22.

[30] S. Bochkarev, S. Lekomtsev, V. Matveenko, Natural vibrations of loaded noncircular cylindrical shells containing a quiescent fluid, Thin-Walled Structures 90 (2015) 12–22.

[31] S. A. Bochkarev, S. V. Lekomtsev, V. P. Matveenko, Dynamic analysis of partially filled non-circular cylindrical shells with liquid sloshing, International Journal of Applied Mechanics 8 (03) (2016) 1650027.

[32] A. Lakis, G. Bursuc, M. Toorani, Sloshing effect on the dynamic behavior of horizontal cylindrical shells, Nuclear Engineering and Design 239 (7) (2009) 1193–1206.

[33] A. Selmane, A. Lakis, Vibration analysis of anisotropic open cylindrical shells subjected to a flowing fluid, Journal of Fluids and Structures 11 (1) (1997) 111–134.

[34] F. Sabri, A. A. Lakis, Hydroelastic vibration of partially liquid-filled circular cylindrical shells under combined internal pressure and axial compression, Aerospace Science and Technology 15 (4) (2011) 237–248.

[35] A. Ergin, W. Price, R. Randall, P. Temarel, et al., Dynamic characteristics of a submerged, flexible cylinder vibrating in finite water depths, Journal of ship research 36 (02) (1992) 154–167.

[36] E. Ventsel, V. Naumenko, E. Strelnikova, E. Yeseleva, Free vibrations of shells of revolution filled with a fluid, Engineering analysis with boundary elements 34 (10) (2010) 856–862.

[37] M. E. Yildizdag, I. T. Ardic, M. Demirtas, A. Ergin, Hydroelastic vibration analysis of plates partially submerged in fluid with an isogeometric FE-BE approach, Ocean Engineering 172 (2019) 316–329.

[38] A. Ergin, P. Temarel, Free vibration of a partially liquid-filled and submerged, horizontal cylindrical shell, Journal of Sound and vibration 254 (5) (2002) 951–965.

[39] C.-J. Zheng, C.-X. Bi, C. Zhang, H.-F. Gao, H.-B. Chen, Free vibration analysis of elastic structures submerged in an infinite or semi-infinite fluid domain by means of a coupled FE-BE solver, Journal of Computational Physics 359 (2018) 183–198.

[40] T. J. Hughes, J. A. Cottrell, Y. Bazilevs, Isogeometric analysis: CAD, finite elements, NURBS, exact geometry and mesh refinement, Computer

methods in applied mechanics and engineering 194 (39-41) (2005) 4135–4195.

[41] A. Cazzani, M. Malagù, E. Turco, Isogeometric analysis: a powerful numerical tool for the elastic analysis of historical masonry arches, Continuum Mechanics and thermodynamics 28 (1-2) (2016) 139–156.

[42] A. Cazzani, M. Malagù, E. Turco, F. Stochino, Constitutive models for strongly curved beams in the frame of isogeometric analysis, Mathematics and Mechanics of Solids 21 (2) (2016) 182–209.

[43] A. Cazzani, M. Malagù, E. Turco, Isogeometric analysis of plane-curved beams, Mathematics and Mechanics of Solids 21 (5) (2016) 562–577.

[44] A. Cazzani, F. Stochino, E. Turco, An analytical assessment of finite element and isogeometric analyses of the whole spectrum of Timoshenko beams, ZAMM-Journal of Applied Mathematics and Mechanics/Zeitschrift für Angewandte Mathematik und Mechanik 96 (10) (2016) 1220–1244.

[45] A. Kefal, K. A. Hasim, M. Yildiz, A novel isogeometric beam element based on mixed form of refined zigzag theory for thick sandwich and multilayered composite beams, Composites Part B: Engineering 167 (2019) 100–121.

[46] M. E. Yildizdag, M. Demirtas, A. Ergin, Multipatch discontinuous Galerkin isogeometric analysis of composite laminates, Continuum Mechanics and Thermodynamics (2018) 1–14.

[47] K. A. Hasim, A. Kefal, E. Madenci, Isogeometric plate element for unstiffened and blade stiffened laminates based on refined zigzag theory, Composite Structures 222.

[48] I. Temizer, Multiscale thermomechanical contact: Computational homogenization with isogeometric analysis, International journal for numerical methods in engineering 97 (8) (2014) 582–607.

[49] S. Nishi, K. Terada, I. Temizer, Isogeometric analysis for numerical plate testing of dry woven fabrics involving frictional contact at meso-scale, Computational Mechanics 64 (1) (2019) 211–229.

[50] A. Bartezzaghi, L. Dedè, A. Quarteroni, Biomembrane modeling with isogeometric analysis, Computer Methods in Applied Mechanics and Engineering 347 (2019) 103–119.

[51] B. Bastl, M. Brandner, J. Egermaier, K. Michálková, E. Turnerová, Isogeometric analysis for turbulent flow, Mathematics and Computers in Simulation 145 (2018) 3–17.

[52] M. Chen, G. Jin, T. Ye, Y. Zhang, An isogeometric finite element method for the in-plane vibration analysis of orthotropic quadrilateral plates with general boundary restraints, International Journal of Mechanical Sciences 133 (2017) 846–862.

[53] Y. Xue, G. Jin, H. Ding, M. Chen, Free vibration analysis of in-plane functionally graded plates using a refined plate theory and isogeometric approach, Composite Structures 192 (2018) 193–205.

[54] G. Jin, Y. Xue, C. Zhang, T. Ye, K. Shi, Interior two-dimensional acoustic modelling and modal analysis using isogeometric approach, Journal of Sound and Vibration 453 (2019) 103–125.

[55] S. Khakalo, J. Niiranen, Isogeometric analysis of higher-order gradient elasticity by user elements of a commercial finite element software, Computer-Aided Design 82 (2017) 154–169.

[56] J. J. Alibert, P. Seppecher, F. dell'Isola, Truss modular beams with deformation energy depending on higher displacement gradients, Mathematics and Mechanics of Solids 8 (1) (2003) 51–73.

[57] F. dell'Isola, U. Andreaus, L. Placidi, At the origins and in the vanguard of peridynamics, non-local and higher-gradient continuum mechanics: An

underestimated and still topical contribution of Gabrio Piola, Mathematics and Mechanics of Solids 20 (8) (2015) 887–928.

[58] I. Giorgio, F. dell'Isola, D. Steigmann, Axisymmetric deformations of a 2nd grade elastic cylinder, Mechanics Research Communications 94 (2018) 45–48.

[59] F. dell'Isola, P. Seppecher, J. J. Alibert, T. Lekszycki, R. Grygoruk, M. Pawlikowski, D. Steigmann, I. Giorgio, U. Andreaus, E. Turco, et al., Pantographic metamaterials: an example of mathematically driven design and of its technological challenges, Continuum Mechanics and Thermodynamics 31 (4) (2019) 851–884.

[60] F. dell'Isola, P. Seppecher, M. Spagnuolo, E. Barchiesi, F. Hild, T. Lekszycki, I. Giorgio, L. Placidi, U. Andreaus, M. Cuomo, et al., Advances in pantographic structures: design, manufacturing, models, experiments and image analyses, Continuum Mechanics and Thermodynamics (2019) 1–52.

[61] J. Maestre, I. Cuesta, J. Pallares, An unsteady 3D isogeometrical boundary element analysis applied to nonlinear gravity waves, Computer Methods in Applied Mechanics and Engineering 310 (2016) 112–133.

[62] K. V. Kostas, A. I. Ginnis, C. G. Politis, P. D. Kaklis, Shape-optimization of 2D hydrofoils using an isogeometric BEM solver, Computer-Aided Design 82 (2017) 79–87.

[63] X. Wang, S. P. Chouliaras, P. D. Kaklis, A. A.-I. Ginnis, C. G. Politis, K. V. Kostas, et al., Wave-resistance computation via CFD and IGA-BEM solvers: A comparative study, in: The 27th International Ocean and Polar Engineering Conference, International Society of Offshore and Polar Engineers, 2017.

[64] D. F. Rogers, An introduction to NURBS: with historical perspective, Elsevier, 2000.

[65] L. Piegl, W. Tiller, The NURBS book, Springer Science & Business Media, 2012.

[66] R. Echter, B. Oesterle, M. Bischoff, A hierarchic family of isogeometric shell finite elements, Computer Methods in Applied Mechanics and Engineering 254 (2013) 170–180.

[67] J. A. Cottrell, T. J. Hughes, Y. Bazilevs, Isogeometric analysis: toward integration of CAD and FEA, John Wiley & Sons, 2009.

[68] A. Ergin, B. Ugurlu, Hydroelastic analysis of fluid storage tanks by using a boundary integral equation method, Journal of Sound and Vibration 275 (3-5) (2004) 489–513.

[69] G. Beer, I. Smith, C. Duenser, The boundary element method with programming: for engineers and scientists, Springer Science & Business Media, 2008.

Conflict of Interest

No potential conflict of interest was reported by the authors.

Author Statement

M.E.Y. developed the model, performed the computations, and prepared Sections 4 and 5. I.T.A. carried out the experimental measurements and prepared Sections 1 and 3. A.K. prepared Section 2. A.E. supervised the study.